Late Oligocene-Miocene proto-Antarctic Circumpolar Current dynamics off the Wilkes Land margin, East Antarctica

Dimitris Evangelinos[a], Carlota Escutia[a], Johan Etourneau[a,b,c], Frida Hoem[d], Peter Bijl[d], Wilrieke Boterblom[d], Tina van de Flierdt[e], Luis Valero[f], José-Abel Flores[g], Francisco J. Rodriguez-Tovar[h], Francisco J. Jimenez-Espejo[a], Ariadna Salabarnada[a], and Adrián López-Quirós[a].

[a] Instituto Andaluz de Ciencias de la Tierra, CSIC-Univ. de Granada, Av. de las Palmeras, 4, 18100, Armilla, Spain
[b] EPHE, PSL University, Paris, France.
[c] UMR 5805 EPOC CNRS, University of Bordeaux, Bordeaux, France.
[d] Palaeoecology, Institute of Environmental Biology, Faculty of Science, Laboratory of Palaeobotany and Palynology, Utrecht, University, Budapestlann, 4, 3584 CD, Utrecht, The Netherlands.
[e] Department of Earth Sciences and Engineering , South Kensington Campus, London SW7 2AZ, United Kingdom.
[f] Département des Sciences de la Terre, Université de Genève, Rue des Maraîchers 13, 1205 Geneva, Switzerland.
[g] Department of Geology, University of Salamanca, 37008, Salamanca, Spain.
[h] Departamento de Estratigrafía y Paleontología, Facultad de Ciencias, Universidad de Granada, 18002, Granada, Spain.

Keywords: ACC, CDW, Wilkes Land, DSDP 269, Late Oligocene- Miocene

ABSTRACT

At present, the Southern Ocean plays an important role in the global climate system and in modern Antarctic ice sheet dynamics. Past Southern Ocean configurations are however poorly understood. This information is yet important as it may provide important insights into the climate system and past ice-sheet behavior under warmer than present day climates. Here we study Southern Ocean dynamics during the Oligocene and

Miocene when reconstructed atmospheric CO_2 concentrations were similar to those expected during this century. We reconstruct snapshots of late Oligocene to earliest Miocene (~24.2–23 Ma) paleoceanographic conditions in the East Antarctic Wilkes Land abyssal plain. For this, we combine marine sedimentological, geochemical (X-ray fluorescence, TEX_{86},), palynological and isotopic (ε_{Nd}) records from ocean sediments recovered at Deep Sea Drilling Project (DSDP) Site 269. Overall, we find that sediments, delivered to the site by gravity flows and hemipelagic settling during glacial–interglacial cycles, were persistently reworked by a proto-Circumpolar Deep Water (CDW) with varying strengths that result from climatically controlled frontal system migrations. Just prior to 24 Ma, terrigenous input of predominantly fine-grained sediments deposited under weak proto-CDW intensities and poorly ventilated bottom conditions dominates. In comparison, 24 Ma marks the start of episodic events of enhanced proto-CDW current velocities, associated with coarse-grained deposits and better-ventilated bottom conditions. In particular, the dominance of P-cyst and low Calcium (Ca) in the sediments between ~24.2 Ma and 23.6 Ma indicate the presence of an active open ocean upwelling associated with high nutrient conditions. This is supported by TEX_{86}-derived sea surface temperature (SST) data pointing to cool ocean conditions. From ~23.6 to 23.2 Ma, our records reveal an enrichment of Ca in the sediments related to increased calcareous microfossil preservation, high amounts of G-cysts and increasing TEX_{86}-SSTs. This implies warmer water masses reaching the Antarctic margin as the polar front migrated southward. Together with the radiogenic Nd isotope data indicating modern-like CDW values, our records suggest a prominent poleward expansion of proto-CDW over our study site and reduced AABW formation during the latest Oligocene (i.e. ~23.2 Ma ago). Our findings support the notion of a fundamentally different Southern Ocean, with a weaker proto-ACC than present during the late Oligocene and the earliest Miocene.

1. Introduction

The Antarctic Circumpolar Current (ACC) is the Earth´s strongest ocean current (137-162 sverdrup (Sv)) flowing eastward along a 20,000 km pathway around Antarctica (Rintoul et al., 2001; Sokolov and Rintoul, 2009). Owing to the absence of land barriers, the ACC is the only ocean current connecting the Pacific, the Atlantic and the Indian oceans, and consequently influences the entire global ocean circulation (Rintoul, 2018). The ACC pathway is constrained by ocean gateways (i.e. Drake Passage) and the bathymetry of the Southern Ocean. Its strength is mainly controlled by the seafloor topography (Olbers et al., 2004), and the position and intensity of the Southern Westerly Winds (SWW) (Thompson and Solomon, 2002, Aoki et al., 2005; Toggweiler and Russell, 2008; Rignot et al., 2019). At present, the vigorous zonal flow of the ACC prevents the intrusion of warm waters from lower latitudes to penetrate the Antarctic margin and, together with sea-ice presence, contributes to maintain the cold and arid glacial state of Antarctica (e.g., Olbers et al., 2004; Ferrari et al., 2014). The deep layers of the ACC are occupied by a relatively warm and saline water mass, the Circumpolar Deep Water (CDW) (Orsi et al., 1995). Recently, an increasing incursion of CDW into the continental margins has been shown to favor melting and thinning of the Antarctic ice shelves through basal melting (Pritchard et al., 2012; Liu et al., 2015; Nakayama et al., 2018; Rignot et al., 2019). Despite its importance for the Antarctic and the global climate, little is known about the onset and past dynamics of the ACC, as well as its linkages with the Antarctic Ice sheet (AIS) dynamics. This knowledge is especially relevant from past times when climatic conditions were close to the modern and future ones in terms of warmth and atmospheric CO_2 concentration.

One of these times was the late Oligocene (i.e., ~24.5 Ma), when the reconstructed atmospheric CO_2 concentrations dropped below 600 ppm (600-400 ppm) (Zhang et al., 2013). These values are similar to the modern and projected atmospheric CO_2 concentrations within this century (IPCC, 2013; Meredith et al., 2019). Foster and Rohling (2013) argued that the global ice volume is supposedly less sensitive to CO_2 fluctuations between 600 to 400 ppm. In contrast, benthic foraminiferal oxygen isotope records (e.g., Liebrand et al., 2017) suggest highly fluctuating ice volumes at this time. The drop in CO_2 concentration in the late Oligocene (~24.5 Ma) likely led to climate cooling and ice sheet advance across the Antarctic continental shelves, connecting large areas of marine-based ice with the ocean (Pekar and Christie-Blick, 2008; Levy et al., 2019). Ice-proximal geological records (Barrett, 1975; Naish et al., 2008; Kulhanek et al., 2019; Levy et al., 2019) and seismic data (Anderson and Bartek, 1992; Sorlien et al., 2007) provide direct evidence for a major expansion of marine ice sheets across the Ross Sea continental shelf between 24.5 and 24 Ma. However, the oceanographic and climatic conditions leading to the maximum growth of the ice sheet remain poorly known.

The global deep-sea benthic $\delta^{18}O$ records maximum expansion of the AIS between 23.2 and 23 Ma (Zachos et al., 2001; Beddow et al., 2016; Liebrand et al., 2017). However, deep-sea benthic $\delta^{18}O$ records reflect a combination of ice-volume and bottom water temperature and their location (low to mid-latitude versus Antarctic proximal records) determines the different water masses influencing the record and thus masking information from the Antarctic glaciation (e.g., Pekar et al., 2006). Thus, most of the ice volume estimates based on deep-sea benthic $\delta^{18}O$ records should be taken with caution. Variations in the Southern Ocean circulation and ocean heat transport across the Antarctic continental margin driven by obliquity forcing have been suggested to play a significant role on ice sheet sensitivity during the late Oligocene and Miocene (Salabarnada et al., 2018; Sangiorgi et al., 2018; Levy et al., 2019). This is especially true in times when ice sheets extended into the marine environments (e.g., Jovane et al., 2019; Levy et al., 2019). Sedimentary archives strategically located along latitudinal transects across the main ACC pathway and at the vicinity of the Antarctic ice sheet are however needed to provide direct links between changes in the ocean circulation and ice sheet dynamics (Escutia et al., 2019).

Sedimentary records across the Tasman Gateway (Pfuhl and McCave, 2005) and from the South Pacific (Lyle et al., 2007) document a shift to higher velocity bottom currents between 25-23 Ma. This shift has been interpreted to result from the onset of a strong, deep-reaching ACC during the late Oligocene. However, recent comparisons between the dinocysts preserved in sediments from the Integrated Ocean Drilling Program (IODP) Site U1356 off the East Antarctic Wilkes Land margin and strata from Tasmania and south of New Zealand indicate a weaker than present day ACC, at least until the middle Miocene (Bijl et al., 2018b). Oligocene and Miocene paleoceanographic reconstructions off the Wilkes Land margin based on sedimentological data (Salabarnada et al., 2018), dinoflagellate biogeography (Bijl et al., 2018a, b; Sangiorgi et al, 2018) and temperature reconstructions (Hartman et al., 2018) suggest a different oceanographic configuration from that of today in this part of the Southern Ocean. These authors report from multiple lines of evidence warm-temperate sea surface temperatures (SST), limited sea ice expansion and reduced formation of Antarctic bottom waters, linked to a weaker oceanic frontal system, which allowed the intrusion of warmer waters from low latitudes towards the Antarctic margin. These data are consistent with Oligocene numerical simulations, which show weaker global overturning and gyre circulation because of weaker SWW (Herold et al, 2012). In addition, modeling results indicate a limited throughflow of the ACC due to the Australasian paleogeography during the Oligocene (Hill et al., 2013).

To decipher the characteristics and dynamics of the ACC and CDW that can then be related to East Antarctic Ice Sheet (EAIS) behavior off Wilkes-Adélie Land during the late Oligocene-Miocene, we report new data from a sediment record recovered by the Deep Sea

Drilling Project (DSDP) Leg 28 at Site 269. This site was drilled on the Wilkes Land abyssal plain (Hayes et al., 1975) along the main pathway of the ACC. We focus on the study of the late Oligocene to earliest Miocene (~24.2-23 Ma) record. This record is partly compromised by debris flows at IODP Site U1356, located on the continental rise (Escutia et al., 2011), ~280 km landward from Site 269, and is missing in most sedimentary archives around the rest of Antarctica. Because of discontinuous drilling at Site 269, we investigate snapshots of the late Oligocene and early Miocene. Sediment, palynological, geochemical and isotopic data are used to describe and characterise the main changes in sedimentation related to proto-CDW dynamics. The findings at DSDP Site 269 are then compared to results from IODP Site U1356 (Escutia et al., 2011, 2014; Salabarnada et al., 2018) (Fig. 1). This latitudinal comparison provides important insights into changes in proto-ACC dynamics that can in turn be related to the evolution of the ice sheet in this region of the East Antarctic margin.

2. Site description and oceanographic setting

DSDP Leg 28 Site 269 is located on the abyssal plain off the Wilkes Land (61°40.57´S, 140°04.21´E, 4282 m water depth) (Hayes et al., 1975) (Fig. 1). Two holes were discontinuously drilled at this site. Our study focuses on Hole 269A, specifically the interval between 655 to 956 meters below sea floor (mbsf) (cores 7R to 13R). Recovered sediments were interpreted shipboard to be mostly turbidites, but evidence of winnowing by bottom currents was also documented (Hayes et al., 1975). Facies were identified within the frame of the DSDP Leg 28 expedition mainly based on the lithology, bioturbation and bed contacts (Piper and Brisco, 1975).

At present, Site 269 is located between the modern southern branch of the Polar Front (PF) and the northern branch of the Southern ACC Front (SACCF). In comparison, Site U1356

(63°18.6138´S, 135°59.9376´E, 3992 m water depth) lies south of the SACCF, near the Antarctic Divergence (Sokolov and Rintoul, 2002) (Fig. 1). Both sites are today covered by the Adélie Land Bottom Water (ALBW) (Rintoul, 1998), which forms in winter time along the Adélie-Wilkes Land Coast (Orsi et al., 1995). Our reconstruction of the paleoposition of Site 269 and Site U1356 is adapted from G-plates geodynamic modeling (http://www.gplates.org; Müller et al., 2018), and uses the plate circuit of Seton et al. (2012). It shows that Site 269 has migrated south since the Oligocene but remained located at ~60°S between the late Oligocene-early Miocene, while the paleolatitude of Site U1356 was around 62°S. Geological evidence derived from the analysis of microfossil assemblages from sedimentary records around Antarctica suggest that the proto-Polar Front (PF) was situated close to 60°S between the late Oligocene-early Miocene (Nelson and Cooke, 2001; Cooke et al., 2002).

Figure 1 near here.

3. Revising the initial age model

We established a new age model based on the integration of new magnetostratigraphic data, dinocyst and calcareous nannofossil biostratigraphy, calibrated using the GTS 2012 Astronomic Age Model (Gradstein et al., 2012) (Figs. 2; S1; S2 and Tables S1; S2). The presence of *Operculodinium janduchenei* in the sediment between ± 753-955 (mbsf) (Cores 9R 3W to 13R) is assigned to the lower Southern Ocean Dinocyst Zone (SODZ) SODZ8 (Bijl et al., 2018a). This suggests that the bottom of Hole 269A cannot be older than late Oligocene (24.2 Ma). Moreover, the last occurrence of *Operculodinium janduchenei* between 753.27-752.32 mbsf (9R 3W 125-129 cm - 9R 3W 30-33 cm) marks the boundary between dinocysts zones SODZ8 and SODZ9. This boundary is calibrated to 23.6 Ma at U1356 (Bijl et al., 2018a) and is correlated to the reversed polarity found at the bottom of chron C6C (C6Cr). This is corroborated by the presence of *Cyclicargolithus abisectus* at 752.9 mbsf indicating that this interval corresponds to the zone NP 25 (Martini, 1971), which implies a latest Oligocene age. The latter however, must be taken with caution given the scarce amount of calcareous nannofossils, as well as the absence of other conventional markers. The presence of *Impagidinium aculeatum* at 658.82 mbsf (7R 4W 30-34 cm) is assigned to the mid- of SODZ10 or older (~23 Ma) (Bijl et al., 2018a). This is correlated with the normal polarity of the geomagnetic chron C6n.2n suggesting also an age of 23 Ma. In addition, based on the biostratigraphic datums we assigned the paleomagnetic reversal at ~ 857.5 mbsf to chron C7n.1n (24 Ma) and at ~703 mbsf to chron C6n.3n (23.23 Ma). Our updated age model suggests an age range for the studied interval from ~24.2 to ~23 Ma (Fig. 2). Initial shipboard data had dated this interval to be of middle Eocene to early Oligocene age (Hayes et al., 1975). We acknowledge that the age model still has large uncertainties due to discontinuous coring, incomplete recovery and the low preservation of microfossils. However, the integration of the well-established Southern Ocean Oligocene-Miocene dinocyst stratigraphy, which was developed at the nearby Site U1356 along with the good correspondence with the magnetostratigraphic data allow us to be relatively confident in our age model.

Figure 2 near here.

4. Methods

4.1 Facies analysis

A detailed facies analysis was performed on sediment from Hole 269A to determine depositional processes and aid paleoenvironmental reconstructions. We conducted a detailed description of the cores using standard sedimentological techniques (i.e., lithological characterization, contacts, sedimentary structures and textures) in order to produce the lithostratigraphic log in Figure 3 and Supplementary Figure 3. Visual descriptions were aided by high-resolution digital images obtained on the archive halves using a Nikon 60mm camera lens mounted on a custom-built line scanner at the Coast Gulf Repository (CGR), in College Station (Texas, USA). High-resolution images were also used for ichnological analysis (i.e., type and degree of bioturbation) performed to characterise the paleoenvironmental conditions prevailing in the seafloor. Ichnological analysis was based on the digital treatment of the high-resolution images following previous researches (Dorador and Rodríguez-Tovar, 2014, 2018; Dorador et al., 2014a, 2014b; Rodríguez-Tovar and Dorador, 2015). It was conducted at the Department of Stratigraphy and Paleontology at the University of Granada (Spain). Further characterisation of the biogenic and terrigenous material within each of the lithofacies defined was achieved by: 1) Bulk grain-size analyses that was performed at EPOC (Environnements et Paléoenvironnements Océaniques et Continentaux) (Bordeaux, France). In total 44 sediment samples (dried overnight in an oven at 40ºC) were measured in a laser microgranulometer Malvern mastersizer hydro 2000G with automatic samples (0.020 to 2000 μm). 2) Wet sieving and High-Resolution Scanning Electron Microscope (HR-SEM) analysis conducted at the Instituto Andaluz de Ciencias de la Tierra, (CSIC, Spain) and at the Centro de Instrumentación Científica (University of Granada, Spain), respectively. Moreover, continuous measurements of magnetic susceptibility (MS) were taken from the archive half sections of the core. For this, the core sections were left out of the refrigerator overnight to acquire a room temperature before scanning. MS measurements were taken every 2 cm using a Bartington MS2 mounted in a Geotek Multi-Sensor Core Logger (MSCL) at the GCR. Core void measurements were removed from the data set.

4.2 Major and Trace Element content

The elemental composition of sediments derived from X-Ray Fluorescence (XRF) core scanners has been used as an indicator of past climate changes in proximal and distal records from the Antarctic margin. For example, titanium (Ti), aluminium (Al), iron (Fe) versus calcium (Ca) have been interpreted to show changes between terrigenous and biogenic $CaCO_3$ deposition (e.g., Grützner et al., 2005; Hepp et al., 2006; Escutia et al., 2009; Salabarnada et al., 2018). In addition, zirconium-based proxies (e.g. Zr/Ti ratios) have previously been used as an indicator of semiquantitative assessment of bottom current velocities in Oligocene sediments from Site U1356 off Wilkes Land (Salabarnada et al., 2018). This is based on the relative enrichment of heavy minerals such as zircon over less dense minerals (e.g., aluminosilicates) that result from hydrodynamic winnowing and sorting of heavy minerals (e.g., Bahr et al., 2014). Bromine (Br)/Ti ratios have been used as indicator of organic matter in the sediments (Bahr et al., 2014; Salabarnada et al., 2018). The Br content is associated to total organic carbon (TOC) concentration in the sediments (Seki et al., 2019), and TOC is mainly related to changes in productivity (organic carbon flux in the sediments) and/or changes in the redox state of the sediment (e.g., Jimenez-Espejo et al., 2007). Br is not biased by lithological changes (i.e. mudstones/sandstones), but is affected by organic matter degradation (Bahr et al, 2014).

XRF core scanning measurements were conducted at 10kV and 30 kV on the archive split sections from Cores 7R to 13R using an Avaatech XRF core scanner at the GCR. The surface of core sections was cleaned carefully for any gypsum and salts, which might have precipitated and then adjusted manually to form an even surface. A 4µm thick ultralene plastic film was used to cover the core surface in order to avoid contamination while scanning. Due to the presence of cracks in many core sections, spot measurements were taken rather than scan the section continuously.

To decipher the different processes influencing the geochemical composition of the sediment, we conducted a Principle Component Analysis (PCA). We used the PAST version 2.10 software package (Hammer et al., 2001) following the data pre-treatment in Bahr et al. (2014), including normalization of the data to reduce the signal artefacts related to changes in lithology. For the PCA, we only selected and show elements with a robust signal quality, i.e., Al, Si, K, Ca, Ti, Fe, Ba, Br, Rb, Sr, and Zr. In this study we report on the following elements and elemental ratios Ca, Ti, Zr/Ti ratios and Br/Ti ratios.

4.3 Neodymium isotopes

Neodymium (Nd) is delivered to the ocean through the weathering of continental crust, and by exchange with sediment on the continental margin (known as boundary exchange; e.g., Frank et al., 2002, Wilson et al., 2013). Consequently, water masses forming in different geological basins will be isotopically distinct. Because of its short oceanic residence time in the ocean (~400-1,000 yr) relative to oceanic mixing (1,500 yr) (Tachikawa et al., 2003) records of Nd isotopes allow us to reconstruct past ocean circulation and changes in the weathering inputs. Neodymium isotopes in fossil fish debris are a robust tool to reconstruct changes in ocean circulation by identifying distinct water masses (e.g. Goldstein and Hemming, 2003; Martin and Scher, 2004; van de Flierdt et al., 2016). Neodymium is incorporated into the fish teeth during the fossilization processes at the sediment-water interface and reflects the isotopic composition of seawater in contact with the seafloor at the time of fish tooth deposition, remineralisation and burial (Shaw and Wasserburg, 1985). Neodymium isotope ratios in fossil fish teeth are considered to be resistant to changes in post-burial alteration (Martin and Scher, 2004; Scher et al., 2011). Neodymium isotope ratios ($^{143}Nd/^{144}Nd$) are expressed as ε_{Nd}, which denotes the deviation of a measured $^{143}Nd/^{144}Nd$ ratio from the chondritic uniform reservoir in parts per 10,000 (DePaolo and Wasserburg, 1976; Jacobsen and Wasserburg, 1980).

Fish debris was handpicked from the >63 μm sediment fractions that were prepared by wet sieving. Four samples were prepared for fish-tooth and bone debris Nd isotope analyses in the MAGIC laboratories at Imperial College London following the sample preparation detailed in supplementary materials. In addition, to account for a potential influence of the detrital sediment towards the Nd isotope composition of pore waters or overlying bottom water, we also measured the Nd isotope compositions of two detrital sediment samples. Sample preparation for these analyses was conducted in the MAGIC laboratories at Imperial College London as detailed in supplementary materials. The detrital samples were processed using the same ion chromatography as the fish debris.

Neodymium isotope ratios for fish debris and detrital sediment samples were determined on a Nu Plasma multiple collector inductively coupled plasma mass spectrometer (MC-ICP-MS) at Imperial College London, operated in static mode. Instrumental mass bias was corrected using the $^{146}Nd/^{144}Nd$ ratio of 0.7219. A JNdi-1 isotope standard was run after every sample and all reported $^{143}Nd/^{144}Nd$ ratios are corrected to a JNd_i value of 0.512115 (Tanaka et al., 2000) using bracketing standards. External reproducibility was monitored using the JNd_i standards, and accuracy was confirmed by measuring USGS BCR-2 rock standards, which yielded average $^{143}Nd/^{144}Nd$ ratios in agreement with the published BCR-2 $^{143}Nd/^{144}Nd$ ratio of 0.512638±0.000015 (Weis et al., 2006).

To correct for the decay of ^{147}Sm to ^{144}Nd within the fish teeth over time we used Sm and Nd concentrations obtained from two samples, which were in good agreement with $^{147}Sm/^{144}Nd$ ratios reported from fossil fish teeth in other marine sedimentary records (e.g., Martin and Scher, 2006; Moiroud et al., 2013; Huck et al., 2017; Wright et al., 2018). When no values available, an average of 0.1286 from the measured samples was applied to calculate

$\varepsilon_{Nd(t)}$ values. The $^{147}Sm/^{144}Nd$ ratios yielded Nd isotope corrections of 0.19 to 0.21 ε_{Nd} units; (t) denotes samples have been corrected for in situ decay of ^{147}Sm.

4.4 TEX$_{86}$

The TetraEtherindeX of 86 carbon atoms (TEX$_{86}$) is a proxy for sea surface temperature (SST). The TEX$_{86}$ paleothermometer employs the temperature-dependent relative abundance of a suite of thaumarchaeotal membrane lipids; glycerol dibiphytanyl glycerol tetraethers (GDGTs) (Schouten et al., 2002, 2013). In short, this method involves lipid extraction from powdered and freeze-dried sediments using accelerated solvent extraction. Lipid extracts were separated into an apolar, ketone and polar fraction by Al_2O_3 column chromatography using hexane:DCM (9:1), hexane:DCM (1:1) and DCM:MeOH (1:1) as respective eluents. 99 ng of a synthetic C_{46} (mass-to-charge ratio, m/z = 744) GDGT standard was added to the polar fraction, which then was dissolved in hexane:isopropanol (99:1, v/v) to a concentration of ~3 mg ml^{-1} and filtered over a 0.45-μm polytetrafluoroethylene filter. The dissolved polar fractions were injected and analysed by high-performance liquid chromatography–mass spectrometry (HPLC–MS), using the double column technique for improved separation of co-eluding compounds (Hopmans et al., 2015). GDGT peaks in the HPLC chromatograms were integrated using ChemStation software. Several calibrations have been proposed to translate TEX$_{86}$ into SST. We employ the TEX$_{86}$ linear calibration ($SST = 81.5 \times TEX_{86} - 26.6$ with a calibration error of ± 5.2 ∘C) by Kim et al. (2010), to enable adequate comparison to existing data, and following elaborate discussions in Hartman et al. (2018). We provide the GDGT peak areas and R-script in the online supplementary materials.

Before interpreting the TEX$_{86}$ results into SST reconstructions samples with overprint, which may affect the reliability of the SST proxy, must be discarded. Terrestrial GDGT input has been reconstructed using the branched and isoprenoid tetraether (BIT) index (Hopmans et al., 2004) as a proxy. Samples with a high BIT index may be biased by soil- and river-derived GDGTs (Hopmans et al., 2004), although the high BIT index may also stem from a decrease in marine crenarchaeol production, as the BIT index is a closed sum between terrestrial GDGTs and the exclusively marine crenachaeol. Several indices for a potential biased source of GDGTs was investigated and outliers discarded. Namely, methane index (Zhang et al., 2011), flagging overprint by sedimentary methanogenic activity, GDGT-2/GDGT-3 ratio (Taylor et al., 2013), potentially signalling overprint by archaeal communities dwelling deeper into the water column, GDGT-0/Crenarchaeol ratio (Blaga et al., 2009; Damsté et al., 2009; Taylor et al., 2013), flagging overprint by in situ production of isoprenoidal GDGTs in lakes and rivers, and ring index (Zhang et al., 2016), which assesses an overall pelagic character for the different GDGTs within the TEX86 index. High-latitude TEX_{86} SST reconstructions might be skewed towards summer temperatures (Ho et al., 2014; Schouten et al., 2013; Hartman et al., 2018) and potentially incorporate a subsurface signal (0-200 mbsl) (Hernández-Sánchez et al., 2014; Ho and Leapple, 2015). However, there is a general agreement that TEX_{86} captures the relative SST trend (Richey and Tierney, 2016).

4.5 Palynology – dinoflagellate cyst paleoenvironment reconstruction

In total 19 sediment samples (~15g) were processed for palynology and counted at Utrecht University using standard palynological processing and analytical procedures previously described by Bijl et al. (2013; 2018b). Modern dinoflagellate (unicellular planktonic protists) distribution are sensitive to small changes in nutrient availability, SST, salinity, bottom water oxygen, primary productivity and sea-ice cover (Dale, 1996; Prebble et al., 2013; Zonneveld et al., 2013). Approximately 13-16% produce an organic-walled cyst, dinocysts, that can preserve in the fossil record (Head, 1996). Assuming the habitat affinities and feeding strategies of most dinoflagellates can be extrapolated to the fossil assemblages, we can utilize 'deep-time' dinocysts assemblages as a paleoceanographic proxy (Bijl et al., 2013; Crouch et al., 2014; Sluijs et al., 2005). In the Southern Ocean, protoperidinioid (P) cysts originate from hetrotrophic dinoflagellates and proliferate under increased nutrient conditions, while gonyaulacoid (G) cysts originate from autotrophic or mixotrophix dinoflagellates and reflect oligotrophic conditions (Esper and Zonneveld, 2002). Thus, the relative P/G-cyst ratio can indicate glacial/interglacial variability and ocean frontal movement migrations. Today, the surface sediments at Site 269A consists almost exclusively of P-cysts, specifically the sea-ice affiliated species Selenopemphix antarctica (Prebble et al., 2013).

5. RESULTS

5.1. Sedimentation at Hole 269A

Sediment from Hole 269A from 655 to 956 mbsf consists of alternations between bioturbated and laminated intervals of terrigenous-rich sediment (Figs. 3a, 3b, 4 and S3). Textural analyses show a low clay content (4 to 20%), a high silt fraction (40 to 80%) and a sand content between <5 and 60 % (Fig. S3). Microfossil preservation is generally low throughout the study interval. Higher preservation of calcareous microfossils was found in the carbonate-cemented beds (Figs. 3a and 5) and within the sediments between 753.5-702.5 mbsf (~23.6 to 23.23 Ma) (Fig. S4). The higher calcareous carbonate preservation is depicted in Ca peaks in Fig. 3d. Higher preservation of diatoms is also observed in the carbonate-cemented facies (Fig. 5) and in Core 7 (660-655.5 mbsf) (~23 Ma).

The main observed differences within the bioturbated and laminated intervals are the variations in the silt/sand content, ichnological features, including amount of bioturbation, and carbonate content (carbonate-cemented intervals). Based on this, we differentiate the following sedimentary facies (Figs. 3c and 4): (1) Bioturbated silty claystones to clayey siltstones (Bioturbated mudstone; F1a), bioturbated siltstones to sandy siltstones (F2a), and bioturbated carbonate-cemented facies (F3a). (2) Laminated silty claystones to clayey siltstones (Laminated mudstone; F1b), laminated siltstones to sandy siltstones (F2b), and laminated carbonate-cemented facies (F3b).

Figure 3 near here.

Bioturbated facies (F1a, F2a and F3a; Figs. 3c, 4 and 5) generally exhibit a structureless and/or mottled texture. Bioturbation varies from low, dominated by *Chondrites* and *Phycosiphon*, to high with abundant and diverse trace fossils, including *Planolites*, *Thalassinoides*, *Nereites*, *Zoophycos* and likely *Scolicia* (Fig. 4). The occurrence of coarser bioturbated facies (F2a) becomes more frequent up-section starting at 858 mbsf, but is also present in the lowermost part of the site at ~ 955.3 mbsf (Fig. 3c).

Laminated facies (F1b, F2b and F3b; Figs. 3c, 4 and 5) are characterised by faint and/or distinct sub-mm to mm silty-sandy laminations. Laminated intervals can contain a single or a group of laminae with various sedimentary structures, including continuous and discontinuous planar, wavy, lenticular, ripple and cross laminations (e.g., Fig. 4a). Small soft-sedimentary deformation structures such as convoluted, ball and pillow structures are often observed within the laminations (Fig. 4k). Scarce traces of *Chondrites* may be present.

Figure 4 near here.

Despite the diagenetic processes associated with the bioturbated and laminated carbonate-cemented facies (F3a, F3b), thin section analyses integrated with HR-SEM images show preservation of microfossils in both facies, including silicified planktonic foraminifers and diatoms (Figs. 5f-h). This observation is noteworthy since the sediments of the study sections were considered almost barren in microfossil (Hayes et al., 1975). The presence of benthic foraminifera with siliceous test suggests diagenetic dissolution and confirms the biogenic origin of these carbonates (Fig. 5). HR-SEM images reveal that the contact between F3b and F3a is sharp and erosive and inverse grading characterizes F3b (Fig. 5e). In total thirteen carbonate-cemented beds were observed, with the thickest ones at 704.2 mbsf and at 655.3 mbsf (e.g., Figs. 3c and 3d).

Figure 5 near here.

The intercalation of bioturbated and laminated facies is characterized by both gradational and sharp contacts. More than 90 sharp contacts were identified (Fig. S3). A common ichnological feature that appears associated with at the sharp contact between the coarse and the fine-grained facies is the presence of pseudo-borings, characterized by well-defined shapes, undeformed, with sharp contacts, infilled with different material to the host sediment (Figs. 4 d-f).

5.2 Geochemistry at Hole 269A

Down-core variations of Ca content clearly track the 13 carbonate-cemented beds (Fig. 3d). In these beds, the dissolution of calcareous microfossils results in carbonate cementation/re-precipitation, as shown by the HR-SEM analyses (Fig. 5h). Additionally, we observe an interval of increased Ca values within the non-carbonate-cemented sediments between 706.8-703.28 mbsf (~23.23 Ma) (Fig. 3d). This increase is also associated with the preservation, even if scarce, of calcareous microfossils (i.e., planktonic, benthic foraminifers and calcareous nannofossils, Fig. S4).

In comparison, Ti variations show negative excursions in the carbonate-cemented facies (Fig. 3e). Ti decreases after 858 mbsf (~24 Ma), and more pronounced between 752.5 to 655 mbsf (~23.6 to 23 Ma) (Fig. 3e).

A principal component analyses (PCA) yielded one major principal component ($PC1_{TOT}$) that explains 63.8 % of the total variance in the XRF data (Table S4). $PC1_{TOT}$ is characterised by negative loadings for Ca and positive loading for all the other elements (Al, Si, K, Ti, Fe, Br, Ba, Sr, Zr) (Fig. 6a). Prominent negative excursions in $PC1_{TOT}$, are associated with the carbonate-cemented beds. In addition, $PC1_{TOT}$ decreases after 752.5 mbsf (~23.6 Ma) (Fig. S5).

Because of the distinct lithological/geochemical characteristics of carbonate-cemented beds compared to the rest of the sediments in our record, we ran another PCA, excluding the carbonate-cemented sediment. The first PC, named PC1 describes the 34.7% of the total variance, with main negative loadings for Zr and Ca and in lesser degree Sr, Br and Si and positive loading for all the other detrital elements (Al, Si, K, Ti, Fe, Ba, Rb) (Table S3; Fig. 6b). This pattern suggests accumulation of heavy elements (e.g., Zr) due to sediment sorting likely by bottom currents.

Figure 6 near here.

Down-core variations of Zr/Ti ratios show high short-term variability (Fig. 3f). In general Zr/Ti show similar patterns with PC1 (Fig. S5) supporting further that both proxies reflect the accumulation of heavy minerals, due to the sorting of bottom currents and/or gravity flows. Zr/Ti ratios show less pronounced variability in fine-grained sediments between 910.5 and 901 mbsf. In general, above 858 mbsf (~24 Ma), Zr/Ti ratios show higher values (Fig. 3f). At 856.75 and 857.5 mbsf (~24 Ma) two prominent peaks of high Zr/Ti ratios, are recorded in ripple cross-laminated sandy siltstones, which indicate the strongest episodes of bottom current velocities within our study interval (Fig. S5b). In addition, high Zr/Ti ratios are shown between 752.5 to 750.17 mbsf (~23.6 Ma) (Fig. 3f).

Br/Ti ratios also increase slightly above 858 mbsf (~24 Ma). It is however between 752.5 and 655 mbsf (~23.6 Ma and 23 Ma) that ratios show increased values, which coincide with the higher preservation of microfossils in the non-carbonate cemented sediment (Fig. 3g).

The $\varepsilon_{Nd(t)}$ data from fish debris range from -9.03 ± 0.25 to -8.07 ± 0.21 (average $\varepsilon_{Nd(t)}$ values -8.54 ± 0.22) during the late Oligocene (~24 to 23.23 Ma) (Fig. 3h).

Late Oligocene detrital sediment samples from Site 269 have $\varepsilon_{Nd(t)}$ values of -12.14 ± 0.33 and $\varepsilon_{Nd(t)}$= -13.33 ± 0.33, at 854.72 mbsf (~24 Ma) and 751.34 mbsf (~23.6 Ma), respectively, and are within the range of local bedrock composition of proximal areas east of the Metz glacier, within the Wilkes Subglacial Basin (Early Paleozoic granite outcrops; ε_{Nd}= -11.2 and -19.8; Bertram, et al., 2018; Cook et al., 2013; 2017).

5.3 TEX$_{86}$

Of the 15 samples processed, 4 were flagged as outliers with potential for a biased source and thus they were not suitable for TEX$_{86}$ analysis. The remaining 11 samples had normal values in the indices signaling overprints as mentioned in the methods. SST values were calibrated between 9-14°C, ± 5.2$_{o}$C, with bioturbated facies characterized by higher SST values, compared to the laminated facies (Fig. 3i). The relative temperature variability of 3-5°C between laminated and bioturbated sediments, respectively at Hole 269A, is consistent with sedimentological features, glacial-interglacial variability and TEX$_{86}$-derived SST reported from Site U1356 (Hartman et al., 2018; Salabarnada et al., 2018).

5.4 Palynology

All examined samples yielded well to moderately preserved palynomorphs assemblages with *Leiosphaera* (70-80%), in-situ dinocyst (20%) and pollen, while spores and reworked dinocyst are a minor component (Table S2). As is common in high polar latitudes, the absolute abundances of dinocysts remain low throughout the examined succession, and do not exceed 400 cysts/g sediment. Assemblages are dominated by P-cysts, with *Brigantedinium* spp. as most abundant (45-90% of the in situ dinocyst sum), *Lejeunecysta* (<10%) showing no clear trend throughout the section and *Selenopemphix* with its largest abundance at between 955-909 mbsf (30%) (Fig. 3k). Even if less abundant (rarely >5%), the samples yielded a G-cyst assemblage that mainly consists of *Batiacasphaera, Pyxidinopsis, Operculodinium* and *Impagidinium*. Similar G-cyst assemblages are present throughout the Oligocene-Miocene record from the U1356 (Bijl et al., 2018b). G-cyst are notably common between 954.3-950.3 mbsf (~24.2 Ma) and around 23.6 Ma, with additions of *Spiniferites spp*. (sample 9R 3W 125-129 cm) and *G. inflata* (sample 9R 2W 26-30 cm). Bioturbated facies contain more G-cyst compared to the laminated facies (Fig. 3k).

6 DISCUSSION

6.1 Glacial-interglacial sedimentation and short-term polar frontal system dynamics

Repeated alternations between laminated and bioturbated facies like those described at Hole 269A (Figs. 3c and 4), are common in deep-water settings around Antarctica and are interpreted to result from changes in sedimentation related to glacial-interglacial cycles, respectively (e.g., Hepp et al., 2006; Lucchi and Rebesco, 2007; Escutia et al., 2009, 2011; Patterson et al., 2014; Salabarnada et al., 2018).

Terrigenous laminated deposits at Hole 269A (F1b, F2b, Figs. 3c and 4) are interpreted to form by a complex interplay between sediments delivered by gravity flows (e.g., debris flows and turbidity currents) and bottom currents, during glacial times. Even when laminated deposits preserve turbidite affinity (e.g., sharp/erosional bases, normal grading depicted by visual observations and Zr/Ti variability) (e.g., Figs. S6a and S6c), we find evidence suggesting that these intervals were continuously reworked by bottom currents. This evidence include internal structures such as mud drapes, double mud layers, lenticular laminations, mud-offshoots and a rhythmic character between the intercalation of the muddy/sandy couplets with varying thicknesses (e.g., Figs. 4b, e and k). These structures are typical in contourite deposits and are interpreted to indicate both traction and suspension processes during deposition (Shanmugam et al., 1993; Rebesco et al., 2014). Additionally, the absence or scarcity and low diversity of trace fossils such as *Chondrites* and *Phycosiphon* in the laminated facies can suggest a poorly oxygenated/ventilated environment at seafloor, changes in nutrient availability and likely high sedimentation rates that promote unfavorable conditions for trace markers to thrive (e.g., Lucchi and Rebesco, 2007; Rodríguez-Tovar and Dorador, 2014, Rodríguez-Tovar et al., 2014; 2015a, b, 2019; Hodell et al., 2017). Poorly ventilated conditions at the seafloor where also reported from late Oligocene laminated facies at Site U1356, during glacial times (Salabarnada et al., 2018).

In comparison, bioturbated facies (F1a, F2a, Figs 3c and 4) are interpreted to result from mainly hemipelagic sedimentation during interglacial times with continued reworking by bottom currents. The inverse and bi-gradational grading patterns shown by Zr/Ti ratios and MS variations, when resolution is sufficient (Fig. S6) is a strong evidence of bottom current control, suggesting winnowing by bottom currents with fluctuating intensities (e.g., Stow and Faugéres, 2008). The diverse trace fossil assemblage, indicate more oxygenated/better ventilated conditions, likely higher nutrient content in the seafloor and lower sedimentation favorable to microbenthic trace marker proliferation than during glacial times (e.g., Lucchi and Rebesco, 2007; Rodríguez-Tovar et al., 2015a, b). Late Oligocene bioturbated deposits from Site U1356 also record an increase in oxygenation at the seafloor when compared with laminated deposits of the same age at the site (Salabarnada et al., 2018).

The carbonate-cemented laminated and bioturbated facies (facies: F3a, F3b; Figs 3c and 5) are interpreted to result from sedimentation during the warmest interglacials recorded by our sediments. This is indicated by the high Ca content (Fig. 3d) associated with dissolution of calcareous microfossils, which strongly supports the biogenic origin of these carbonate beds (Figs. 5f, 5g and 5h).

Our interpretation of sediments recovered at Site 269 from 956 to 858 mbsf (before 24 Ma) is supported by similar late Oligocene (26-25 Ma) bioturbated and laminated sediments recovered at the more proximal IODP Site U1356. Nearly continuous recovery of this interval at Site U1356, allowed for a detailed study of glacial-interglacial cyclicity that is paced by obliquity (Salabarnada et al., 2018). These authors interpreted the changes between laminated and bioturbated facies at Site U1356 to be driven by oceanic frontal migrations forced by glacial-interglacial cycles. In detail, during interglacial times, southward migration of the SWW and the surface oceanic fronts facilitated proto-CDW intrusions closer to the Antarctic margin. This allowed better preservation of calcareous microfossils and enhanced ventilation at the seafloor. The opposite occurred during the glacial times. In addition, even when the interval from 26 and 25 Ma was generally warm as indicated by the prevalence of open water conditions (Bijl et al., 2018), TEX_{86}-derived SST variations (between 1.5 and 3 ºC) (Hartman et al., 2018) correlate with the glacial-interglacial cyclicity reported by Salabarnada et al. (2018). In fact, our more distal TEX_{86}-based SST data and dinocyst assemblages, compared to those from Site U1356 (Hartman et al., 2018; Bijl et al., 2018b) support further the oceanic frontal migrations forced by glacial-interglacial cycles. The relative SST variability of 3-5°C at Site 269 may be slightly higher than the glacial-interglacial TEX_{86}-derived SST variability from Site U1356 during the Oligocene-Miocene (Hartman et al., 2018), although a full representation of the glacial-interglacial variability at either site might not have been captured. Additionally, the high abundance of *Brigantedinium spp* (P-cyst) reflect open ocean upwelling and high-nutrient conditions (Harland and Pudsey, 1999; Zonneveld et al., 2013) at Site 269, perhaps even more than at U1356. In addition, the lower amounts of G-cysts compared to Site U1356 indicate that Site 269 was located closer to the upwelling/divergence zone during the glacial times. In contrast, SST increase and higher amounts of G-cysts (lower P/G cyst ratios) similar to modern temperate (interglacial), oligotrophic waters from around Tasmania and southern New Zealand (Prebble et al., 2013) indicate the southward migration of the oceanic fronts during the interglacial times. Our results are consistent with dinocyst assemblages at Site U1356, which show similar changes between oligotrophic, temperate dinocyst assemblages during interglacials, to eutrophic, colder dinocysts during glacial times (Bijl et al., 2018b). The difference in dinocyst assemblages between the two sites may be attributed to a closer proximity of Site 269 to the Antarctic Divergence.

Deposition of large stacked debris flow deposits at Site U1356 between ~24.76 Ma and 23.23 Ma (Escutia et al., 2011; Passchier et al., 2018) provide limited information regarding ocean configurations during the late Oligocene-early Miocene in this region of the East Antarctic margin. This gap is recorded at Site 269 despite the limitations related to the discontinuous drilling and low-resolution age model. Our sedimentological, geochemical and palynological analyses show that the climate-related ocean polar frontal movement migrations continued throughout the late Oligocene and into the early Miocene. We also note an increase in the frequency of siltstones and sandstones beds between 24 and 23.23 Ma. These sediments could result from local inputs from structural highs depicted nearby in seismic lines that cross the site (De Santis et al., 2003). We note however that Oligocene and the Miocene deposition around these highs is dominated by contourite deposition forming mounded deposits against the highs (De Santis et al., 2003), which could prevent direct delivery of sediment to where Site 269 is located. The correlations previously established between sedimentation at Sites 269 and U1356, argues for a regional source of sediments to Site 269 rather than a local one. We therefore argue that these coarse sediments likely correspond to the distal reaches of the debris flow deposits recovered at Site U1356. At this site these deposits have been interpreted to result from ice sheet advances into the continental shelf (Escutia et al., 2011, 2014).

6.2 Bottom water signatures at Site 269

Geological evidence derived from microfossil assemblages from sedimentary records around Antarctica, including evidence from Site 269, suggest that the proto-Polar Front (PF) was placed close to 60_{o}S between the late Oligocene-early Miocene (Nelson and Cooke, 2001; Cooke et al., 2002). This is further supported by dinocyst assemblage data from Hole 269A indicating that the site was influenced by nutrient-rich upwelling and ice-free waters, with occasionally southward latitudinal transport of waters during the late Oligocene and early Miocene. Fish debris neodymium isotope results from Site 269 (Fig. 3h) are consistent with late Oligocene proto-CDW $\varepsilon_{Nd(t)}$ values recorded along the proto-PF on the Kerguelen Plateau (Indian Ocean) (average $\varepsilon_{Nd(t)}$ = -7.8; Wright et al., 2018) and around Maud Rise (Atlantic Ocean) (average $\varepsilon_{Nd(t)}$ = -8.5; Scher and Martin, 2004). The combined dataset suggests that a common bottom water mass (proto-CDW) was bathing the South Atlantic and South Indian Ocean along the proto-PF. The pronounced difference between the $\varepsilon_{Nd(t)}$ values of the fish debris and the detrital sediment samples from Site 269 ($\varepsilon_{Nd(t)}$= -12.14 ± 0.33, -13.33 ± 0.33 (~24 Ma and ~23.6 Ma, respectively) confirm the water mass signal in the fish debris samples (Fig. S7). Bathymetric reconstructions show that the Southern Indian Ocean basin was already sufficiently deep during the Oligocene and did not contain any large topographic barriers that prevented the flow of proto-CDW from the Kerguelen Plateau to the abyssal plain off the Australian-Antarctic basin (Scotese and Wright, 2018). Based on the above, we conclude that at least during the latest Oligocene (~24 to ~23.23 Ma), Site 269 was covered by a proto-CDW with a Nd signature similar to the present day CDW in the Australian sector of Southern Ocean (ε_{Nd} = -8.1 to -9.1; Lambelet et al., 2018). This observation contrasts with the present-day bottom water mass configuration at the location of Site 269, which is bathed by Adélie Land Bottom Water (ALBW) (Rintoul, 1998), suggesting a reduced export of ALBW during the late Oligocene. These results are consistent with previous inferences for reduced sea ice in the region (Bijl et al., 2018b; Hartman et al., 2018) diminishing production of ALBW at the Oligocene and Miocene on the Wilkes Land shelf. The less radiogenic $\varepsilon_{Nd(t)}$ value around 24 Ma ($\varepsilon_{Nd(t)}$ = -9.03 ± 0.25) may suggest mixing between proto-CDW and Adélie Coast Bottom Water (ACBW; Oligocene ACBW $\varepsilon_{Nd(t)}$ = - 10.6 ± 0.8; Huck et al., 2017). However, more data are needed to confirm this hypothesis.

6.3 Long-term changes in the proto-ACC dynamics during the late Oligocene to earliest Miocene

We provide new insights into the ocean configuration during four distinct periods between the late Oligocene-early Miocene from ~24.2 to 24 Ma, at ~24 Ma, from ~23.6 to 23.23 Ma, and at ~23 Ma.

A remarkable shift in sedimentation occurs at ~24 Ma (858 mbsf) (Fig. 3a). Before 24 Ma, predominantly fine-grained sediment deposited under enhanced terrigenous inputs and an overall weak proto-CDW. This interpretation is supported by the high Ti values and low Zr/Ti ratios, respectively, and their low variability, in particular between 910 to 901 mbsf (Figs. 3e and 3f). Furthermore, less frequent bioturbated facies and low Br/Ti ratios suggest a less ventilated environment and low nutrient content at the seafloor (Figs. 3b and 3g). The high abundance of G-cyst assemblages between 954.3 to 950.3 mbsf (Fig. 3k), together with high SST (11.5 to 14°C) (Fig. 3i), indicate that the polar front system was located south of the Site 269. However, the concomitant SST drop to 9°C and the absence of G-cysts at 948 mbsf (Figs 3i and 3k) indicate northward migration of the polar front, which likely reached Site 269.

Around 24 Ma, our data document the strongest proto-CDW velocities recorded at Hole 269A during the late Oligocene and earliest Miocene, as indicated by the high Zr/Ti peaks associated with cross-sandy laminated intervals that are not preserved elsewhere in the sedimentary record (Figs. 3f and 4e).

After 24 Ma, there is an increase in the frequency of deposition of coarser-grained material interbedded with fine-grained sediment (Fig. 3a). Overall Zr/Ti ratios are higher suggesting periods of proto-CDW strengthening, with Zr/Ti peaks associated with Ca enrichment (Figs. 3f and 6b). In addition, more abundant and diverse bioturbation (Figs. 3b and 3c) point to episodes of better ventilated bottom conditions, and likely higher nutrient content at the seafloor, as indicated by a small increase in Br/Ti ratios (Fig. 3g). Between ~24 and 23.6 Ma, the frontal system migrated northward, as indicated by the lower SST (9.8-10.8°C) and the dominance of P-cysts, suggesting cool and euthrophic ocean conditions. In addition, the sheer absence of dinocysts may have resulted from low preservation associated to oxidation at sea floor, transport by bottom currents and/or reduced productivity. Given the warmth as reconstructed for the surrounding time intervals (e.g., Bijl et al., 2018b; Hartman et al., 2018), we rule out a permanent ice cover during this time.

<u>Figure 7 near here.</u>

We infer that the observed shift in depositional environment at 24 Ma was driven by atmospheric and oceanic frontal changes. SWW northward migration due to the major expansion of the AIS between 24.5 and 24 Ma (see Levy et al., 2019 for discussion) is thought to have forced the northward migration of the SWW prior to 24 Ma (Fig. 7a and 7c). This would have resulted in a weak proto-CDW, reduced water mass mixing, and a less ventilated seafloor. In contrast, the increase in proto-CDW intensification after 24 Ma, inferred from the higher Zr/Ti amplitudes, likely indicate times when SWW migrated southwards, aligned with the proto-ACC. This promoted enhanced mixing and better ventilation of the seafloor and likely higher organic matter deposition, in times when the AIS retreated. Our SST and dinocyst data further support the warmer temperatures and dominance of G-cysts, which indicate the stronger influence of warm oligotrophic waters.

Between ~23.6 and ~23.23 Ma, sediments record a prominent southward polar frontal system migration, which allowed warmer water to penetrate further southwards (Fig. 7a and 7c). This interval is characterized by high Zr/Ti ratios (at ~23.6 Ma, Fig. 3f), high Ca, high SST (11.5-12.9$_{o}$C) (Fig. 3i) and a reduction in terrigenous input (low Ti values) (Figs. 3d and 3e). In addition, there is higher preservation of calcareous microfossils in some intervals (Fig. S2), and dominance of G-cysts (Fig. 3k), similar to those in modern temperate (interglacial), oligotrophic waters from around Tasmania and southern New Zealand (Prebble et al., 2013), high Br/Ti ratios (Fig. 3g) and a thick carbonate cemented bed at ~23.23 Ma (Fig. 3a). Today, calcareous organisms rarely reach the seafloor within and south of the polar front zone. This is because of the presence of the corrosive (CO_2-rich) Antarctic deep waters (Whitehead and Bohaty 2003 and references therein) and strong upwelling (Olbers et al, 2004), which dissolve calcareous rain. A thick carbonate cemented bed is present at Site U1356 dated at 23.23 Ma (Escutia, et al., 2011). The synchronous deposition of these carbonate-cemented beds at Sites U1356 and 269 strongly supports a wide southward expansion of proto-CDW offshore Wilkes Land at ~23.23 Ma. Our ε_{Nd} data, despite their low resolution, also suggest a greater influence of proto-CDW during this period compared to ~24 Ma (Fig. 3h). Similar processes occur today, when a reduction in the volume of AABW is compensated by the expansion of the

CDW (van Wijk and Rintoul, 2014). Our interpretation is further supported by the absence of sea-ice-related dinocyst species (i.e. *Selenopemphix antarctica*) at both Sites 269 and U1356 (Bijl et al., 2018b), which suggests a weaker than modern sea ice season during the Oligocene and Miocene. In addition, the new SST reconstruction at Site 269, similar to those at Site U1356, report warmer surface water conditions than today and argue for a decrease in the potential formation of Antarctic bottom waters (Hartman et al, 2018).

At ~23 Ma, high Br/Ti ratios indicate an increase in the organic content in the sediment (Fig. 3), coinciding with the first evidence (scarce) of diatoms at Site 269. A shift from calcareous dominated microfossils to siliceous (e.g., diatomaceous and cherty clay sediments) has also been reported at Site U1356 (Escutia et al., 2011, Escutia et al., 2014; Passchier et al., 2018) arguing for a major regional event likely related to the AIS expansion during the early Miocene, northward expansion of the polar front system and more influence of siliceous productivity. This is supported by the high amount of P-cyst at Site 269 at ~23 Ma, which indicate cool, nutrient-rich upwelling conditions (Fig 3k). After 23 Ma, deposition of the thickest carbonate cemented bed would imply this period was followed by a southward migration of the frontal system (Fig. 3a).

In summary, our combined sedimentological, geochemical and palynological data between ~24.2 and ~23 Ma show a dynamic proto-ACC off the Wilkes Land margin during the late Oligocene-Miocene. In addition, the carbonate preservation and low siliceous microfossil preservation at Site 269 (located within the polar front zone) contrasts with modern sedimentation near the Polar Front. This is supported by the presence of oligotrophic, temperate dinocyst assemblages at Sites 269 and U1356 that are similar to the ones found today north of the Polar Front around Tasmania and the Southern New Zealand (Bijl et al., 2018b). Our data therefore suggest a weaker frontal system, characterized by reduced upwelling, which probably allowed southward transport of warm surface waters from lower latitude. This is consistent with numerical modelling results indicating a weaker than present-day proto-ACC (Herold et al., 2012; Hill et al, 2013). These findings argue against the onset of a modern-like ACC during the latest Oligocene (ca 25-23 Ma) based on sedimentary records across the Tasman Gateway (Pfuhl and McCave, 2005) and the South Pacific (Lyle et al., 2007).

7. Conclusions

Our integrated sedimentological, geochemical, isotopic and palynological data sets from DSDP Site 269 provide new insights into the proto-ACC dynamics during the late Oligocene-early Miocene (~24.2 to 23 Ma) off the eastern Wilkes Land margin. We show that sedimentation at Site 269 is controlled by the persistent reworking of gravity flows and hemipelagic sedimentation by proto-CDW that is characterised by fluctuating current intensities driven by the migration of the frontal system in response to climatic changes. We detail four distinct snapshots (from ~24.2 to 24 Ma, at ~24 Ma, from ~23.6 to ~23.23 Ma, and at ~23 Ma) that we link to changes in the proto-ACC and deep proto-CDW dynamics. Just before 24 Ma, fine-grained sediments were deposited under enhanced terrigenous inputs and weak proto-CDW intensities that resulted in low ventilated bottom conditions and probably low organic content and preservation. At 24 Ma, episodic events of stronger proto-CDW current velocities started, associated with coarser-grained deposits, and better ventilated bottom conditions and slightly higher organic matter content. In addition, TEX_{86}-derived SST data varied between 9 to 13.5°C, while the dominance of P -cysts indicate relatively cool ocean temperatures, upwelling and high-nutrient conditions between ~24 and 23.6 Ma. Together, these evidences suggest that the polar front at this time was located near the site. At ~23.6 Ma, and more pronounced at ~23.23 Ma, a prolonged expansion of proto-CDW closer to the Wilkes Land margin is indicated by the higher Ca values, better preservation of calcareous microfossils, higher Br/Ti ratios, high

SST (from 11.5 to 12.9$_{o}$C), high amounts of G-cysts similar to modern temperate and oligotrophic waters, and ε_{Nd} data resembling modern-like CDW ε_{Nd} signature at Site 269. Given that the record between ~24.9 and 23.23 Ma was masked by debris flow deposition at the more proximal IODP Site U1356, our results provide the first record of ocean configuration for this margin for this time interval. When compared with results from Site U1356 and with numerical modelling, our findings support the notion of a fundamentally different Southern Ocean with a weaker proto-ACC than today during the late Oligocene and earliest Miocene. A weaker frontal system permitted the incursion of warm waters from lower latitude closer to the Antarctic margin and the preservation of carbonate. The synchronous deposition of thick carbonate-cemented beds both at Site 269 and U1356 at 23.23 Ma indicates a regional event of poleward proto-CDW expansion.

Acknowledgments

This research used samples provided by the International Ocean Discovery Program (IODP). We thank the staff at the Gulf Coast core repository (GCR) for assistance in core handling and shipping. We also thank David Houpt (GCR) for technical support with the XRF core scanning; Katharina Kreissig, Liam Holder, Barry Coles (Imperial College) and Katrina Kerr (Open University) for laboratory and technical support with the Nd isotopes and REE analyses; Emmanuelle Ducassou, Marie-Claire Perello (EPOC) for laboratory and technical support with the grain-size analyses and Hans Nelson for his helpful discussions and improvement of the English in the manuscript. We also thank Laura De Santis and an anonymous reviewer for their constructive comments, which helped to improve this paper. Funding for this research was provided by the Onassis Foundation – Scholarship ID: F ZL 016-1/2015-2016 and the Spanish Ministry of Science and Innovation (grant CTM2017-89711-C2-1-P), co-funded by the European Union through FEDER funds. PB and FH acknowledge funding through the NWO polar programme grant no ALWPP.2016.001 and the European Research Council starting grant no 802835, OceaNice. This paper is a contribution to the SCAR PAIS Programme.

REFERENCES

Anderson, J. B., and Bartek, L. R., 1992. Cenozoic glacial history of the Ross Sea revealed by intermediate resolution seismic reflection data combined with drill site information, The Antarctic Paleoenvironment: A Perspective on Global Change: Part One, p. 231-263. https://doi.org/10.1029/AR056p0231.

Aoki, S., Bindoff, N.L., Church, J.A., 2005. Interdecadal water mass changes in the Southern Ocean between 30°E and 160°E, Geophys. Res. Lett., 32, L07607. doi:10.1029/2004GL022220.

Bahr, A., Jiménez-Espejo, F.J., Kolasinac, N., Grunert, P., Hernández-Molina, F.J., Röhl, U., Voelker, A.H.L., Escutia, C., Stow, D.A.V., Hodell, D., Alvarez-Zarikian, C.A., 2014. Deciphering bottom current velocity and paleoclimate signals from contourite deposits in the Gulf of Cádiz during the last 140 kyr: An inorganic geochemical approach, Geochem. Geophy. Geosy., 15, 3145-3160. https://doi.org/10.1002/2014GC005356.

Barrett, P.J., 1975. Textural characteristics of Cenozoic preglacial and glacial sediments at Site 270, Ross Sea, Antarctica. Initial Rep. Deep Sea Drilling Project 28, 757–766.

Beddow, H.M., Liebrand, D., A. Sluijs, A., Wade, B.S., Lourens, L.J., 2016. Global change across the Oligocene-Miocene transition: High-resolution stable isotope records from IODP Site U1334 (equatorial Pacific Ocean), Paleoceanography, 31, 81–97. doi:10.1002/2015PA002820.

Bertram, R.A., Wilson, D.J., van de Flierdt, T., McKay, R.M., Patterson, M.O., Jimenez-Espejo, F.J., Escutia, C., Duke, G.C., Taylor-Silva, B.I., Riesselman, C.R., 2018. Pliocene deglacial event timelines and the biogeochemical response offshore Wilkes Subglacial Basin, East Antarctica. Earth and Planetary Science Letters 494, 109-116. https://doi.org/10.1016/j.epsl.2018.04.054.

Bijl, P.K., Bendle, J.A., Bohaty, S.M., Pross, J., Schouten, S., Tauxe, L., Stickley, C.E., McKay, R.M., Rohl, U., Olney, M., Sluijs, A., Escutia, C., Brinkhuis, H., and Expedition 318 Scientists., 2013. Eocene cooling linked to early flow across the Tasmanian Gateway. *Proceedings of the National Academy of Sciences*, *110* (24), pp. 9645-9650.

Bijl, P.K., Houben, A.J.P., Bruls, A., Pross, J., Sangiorgi, F., 2018a. Stratigraphic calibration of Oligocene–Miocene organic-walled dinoflagellate cysts from offshore Wilkes Land, East Antarctica, and a zonation proposal, J. Micropalaeontol., 37, 105–138. https://doi.org/10.5194/jm-37-105-2018.

Bijl, PK., Houben, A.J.P., Hartman, J.D., Pross, J., Salabarnada, A., Escutia, C., Sangiorgi, F., 2018b. Paleoceanography and ice sheet variability offshore Wilkes Land, Antarctica – Part 2: Insights from Oligocene–Miocene dinoflagellate cyst assemblages, Clim. Past, 14, 1015–1033. https://doi.org/10.5194/cp-14-1015-2018.

Blaga, C.I., Reichart, G.-J., Heiri, O., Damsté, J.S.S., 2009. Tetraether membrane lipid distributions in water-column particulate matter and sediments: a study of 47 European lakes along a north–south transect. *Journal of Paleolimnology, 41*(3), 523-540

Carter, P., Vance, D., Hillenbrand, C.D., Smith, J.A., Shoosmith, D.R., 2012. The neodymium isotopic composition of waters masses in the eastern Pacific sector of the Southern Ocean. Geochimica et Cosmochimica Acta, 79, 41–59. https://doi.org/10.1016/j.gca.2011.11.034.

Cook, C.P., Hemming, S.R., van de Flierdt, T., Pierce Davis, E.L., Williams, T., Galindo, A.L., Jiménez-Espejo, F.J., Escutia, C., 2017. Glacial erosion of East Antarctica in the Pliocene: a comparative study of multiple marine sediment provenance tracers. Chem. Geol. 466, 199–218.

Cook, C.P., van de Flierdt, T., Williams, T., Hemming, S.R., Iwai, M., Kobayashi, M., Jimenez-Espejo, F.J., Escutia, C., Gonzalez, J.J., Khim, B.-K., McKay, R.M., Passchier, S., Bohaty, S.M., Riesselman, C.R., Tauxe, L., Sugisaki, S., Galindo, A.L., Patterson, M.O., Sangiorgi, F., Pierce, E.L., Brinkhuis, H., Klaus, A., Fehr, A., Bendle, J.A.P., Bijl, P.K., Carr, S.A., Dunbar, R.B., Flores, J.A., Hayden, T.G., Katsuki, K., Kong, G.S., Nakai, M., Olney, M.P., Pekar, S.F., Pross, J., Rohl, U., Sakai, T., Shrivastava, P.K., Stickley, C.E., Tuo, S., Welsh, K., Yamane, M., 2013. Dynamic behaviour of the East Antarctic ice sheet during Pliocene warmth. Nat. Geosci.6 (9), 765–769. https://doi .org /10 .1038 /ngeo1889.

Cooke, P.J., Nelson, C.S., Crundwell, M.P., Spiegler D., 2002. Bolboforma as monitors of Cenozoic palaeoceanographic changes in the Southern Ocean, Palaeogeography, Palaeoclimatology, Palaeoecology, 188(1), 73-100.

Crouch, E.M., Willumsen, P.S., Kulhanek, D.K., Gibbs, S.J., 2014. A revised Paleocene (Teurian) dinoflagellate cyst zonation from eastern New Zealand. *Review of Palaeobotany and Palynology, 202*, 47-79.

Dale, B., 1996. Dinoflagellate cyst ecology: modeling and geological applications. *Palynology: principles and applications*, 1249-1275.

Damsté, J.S.S., Ossebaar, J., Abbas, B., Schouten, S., Verschuren, D., 2009. Fluxes and distribution of tetraether lipids in an equatorial African lake: constraints on the application of the TEX86 palaeothermometer and BIT index in lacustrine settings. *Geochimica et Cosmochimica Acta, 73*(14), 4232-4249.

DePaolo, Wasserburg, G.L., 1976. Nd isotopic variations and petrogenetic models, Geophys. Res. Lett. 3, 249–252.

De Santis, L., Brancolini, G., & Donda, F., 2003. Seismo-stratigraphic analysis of the Wilkes Land continental margin (East Antarctica): influence of glacially driven processes on the Cenozoic deposition. *Deep Sea Research Part II: Topical Studies in Oceanography*, *50*(8–9), 1563–1594. https://doi. org/10.1016/S0967-0645(03)00079-1

Dorador, J., Rodríguez-Tovar, F.J., 2014. A novel application of digital image treatment by quantitative pixel analysis to trace fossil research in marine cores. PALAIOS 29 (10), 533–538.

Dorador, J., Rodríguez-Tovar, F.J., 2018. High-resolution image treatment in ichnological core analysis: initial steps, advances and prospects. Earth-Sci. Rev. 177, 226–237.

Dorador, J., Rodríguez-Tovar, F.J., IODP Expedition 339 Scientists, 2014a. Digital image treatment applied to ichnological analysis of marine core sediments. Facies 60 (1), 39–44.

Dorador, J., Rodríguez-Tovar, F.J., IODP Expedition 339 Scientists, 2014b. Quantitative estimation of bioturbation based on digital image analysis. Mar. Geol. 349, 55–60.

Escutia, C., Bárcena, M.A., Lucchi, R.G., Romero, O., Ballegeer, A.M., Gonzalez, J.J., Harwood, D.M., 2009. Circum-Antarctic warming events between 4 and 3.5 Ma recorded in marine sediments from the Prydz Bay (ODP Leg 188) and the Antarctic Peninsula (ODP Leg 178) margins, Glob. Planet. Change, 69,170–184. https://doi.org/10.1016/j.gloplacha.2009.09.003.

Escutia, C., Brinkhuis, H., 2014. From Greenhouse to Icehouse at the Wilkes Land Antarctic Margin, in arth and Life Processes Discovered from Subseafloor Environments: A Decade of Science Achieved by the Integrated Ocean Drilling Program (IODP), vol. 7, edited by: Stein, R., Blackman, D.K., Inagaki, F., and Larsen, H.-C., 295–328, Elsevier, Amsterdam.

Escutia, C., Brinkhuis, H., AKlaus, A., and Expedition Scientists, 2011. "IODP Expedition 318 : From Greenhouse to Icehouse at the Wilkes Land Antarctic Margin," no. 12: 15–23. https://doi.org/10.2204/iodp.sd.12.02.2011.

Escutia, C., DeConto, R.M., Dunbar, R., De Santis, L., Shevenell, A, T. Naish, T., 2019. Keeping an eye on Antarctic Ice Sheet stability. *Oceanography* 32(1):32–46, https://doi.org/10.5670/oceanog.2019.117.

Esper, O., Zonneveld, K.A.F., 2002. Distribution of organic-walled dinoflagellate cysts in surface sediments of the Southern Ocean (eastern Atlantic sector) between the Subtropical Front and the Weddell Gyre, Mar. Micropaleotol., 46, 177–208.

Ferrari, R., Jansen, M.F., Adkins, J.F., Burke, A., Stewart, A.L., Thompson, A.F., 2014. Antarctic Sea ice control on ocean circulation in present and glacial climates. Proceedings of the National Academy of Sciences of the United States of America, 111(24), 8753–8758. https://doi.org/ 10.1073/pnas.1323922111.

Foster, G.L., Rohling, E.J., 2013. Relationship between sea level and climate forcing by CO2 on geological timescales, P. Natl. Acad. Sci. USA, 110, 1209–1214, https://doi.org/10.1073/pnas.1216073110.

Frank, M., 2002. Radiogenic isotopes: Tracers of past ocean circulation and erosional input: Reviews of Geophysics, v. 40, doi: 10.1029 /2000RG000094.

Goldstein, S.L., Hemming, S.R., 2003. 6.17 - Long-lived isotopic tracers in oceanography, paleoceanography, and ice-sheet dynamics. In: Holland, H.D, Turekian, K.K. (Eds.), Treatise on Geochemistry. Pergamon, Oxford, pp. 453–489.

Gradstein, F.M., Ogg, J.G., Schmitz, M.D., Ogg, G.M., 2012. The Geologic Time Scale 2012, The Geologic Time Scale 2012, 2, 437–1144.

Grützner, J., Hillenbrand, C.-D., Rebesco, M., 2005. Terrigenous flux and biogenic silica deposition at the Antarctic continental rise during the late Miocene to early Pliocene: implications for ice sheet stability and sea ice coverage. Global and Planetary Change 45, 131–149.

Hammer, Ø., Harper, D.A.T., Ryan, P.D., 2001. PAST: Paleontological statistics software package for education and data analysis, Palaeontol. Electron., 4(1), 9.

Harland, R., Pudsey, C.J., 1999. Dinoflagellate cysts from sediment traps deployed in the Bellingshausen, Weddell and Scotia seas, Antarctica, Mar. Micropaleontol., 37, 77–99.

Hartman, J.D., Sangiorgi, F., Salabarnada, A., Peterse, F., Houben, A.J.P., Schouten, S., Escutia, C., Bijl, P.K., 2018. "Paleoceanography and Ice Sheet Variability Offshore Wilkes Land , Antarctica – Part 3 : Insights from Oligocene – Miocene TEX 86 -Based Sea Surface Temperature Reconstructions," 1275–97.

Hayes, D.E., Frakes, L.A., et al., 1975. Initial Reports of the Deep Sea Drilling Project', vol. 28, U.S. Government Printing Office, Washington, pp. 179-210. doi:10.2973/dsdp.proc.28.107.1975.

Head, M., 1996. Modern dinoflagellate cysts and their biological affinities. *Palynology: principles and applications, 3*, 1197-1248.

Hepp, D.A., Mörz, T., Grützner, J., 2006. Pliocene glacial cyclicity in a deep-sea sediment drift (Antarctic Peninsula Pacific Margin). Palaeogeography, Palaeoclimatology, Palaeoecology 231, 181–198.

Hernández-Sánchez, M.T., Woodward, E.M.S., Taylor, K.W.R., Henderson, G.M., Pancost, R. D., 2014. *Variations in GDGT distributions through the water column in the South East Atlantic Ocean. Geochimica et Cosmochimica Acta, 132, 337–348.* doi:10.1016/j.gca.2014.02.009

Herold, N., Huber, M., Müller, R.D., Seton, M., 2012. "Modeling the Miocene Climatic Optimum : Ocean Circulation" 27 (December 2011): 1–22. https://doi.org/10.1029/2010PA002041.

Hill, D. J., Haywood, A.M., Valdes, P.J., Francis, J.E., Lunt, D.J., Wade, B.S., Bowman, V.C., 2013. Paleogeographic controls on the onset of the Antarctic circumpolar current, Geophys. Res. Lett., 40, 5199–5204. https://doi.org/10.1002/grl.50941.

Ho, S.L., Mollenhauer, G., Fietz, S., Martínez-Garcia, A., Lamy, F., Rueda, G., Schipper, K., Méheust, M., Rosell-Melé, Stein, R., Tiedemann, R. Stein, R., 2014. Appraisal of TEX86 and TEX86L thermometries in subpolar and polar regions. *Geochimica et Cosmochimica Acta, 131*, 213-226.

Ho, S.L., Laepple, T., 2015. Glacial cooling as inferred from marine temperature proxies TEX_{H86} and $U_{K'37}$. Earth and Planetary Science Letters, 409, 15-22. doi: https://doi.org/10.1016/j.epsl.2014.10.033.

Hodell, D.A., Nicholl, J.A., Bontognali, R.R.R., Danino, S., Dorador, J., Dowdeswell, J.A., Einsele, J., Kuhlmann, H., Martrat, B., Mleneck-Vautravers, M.J., Rodriguez-Tovar, F.J., Rohl, U., 2017. Anatomy of Heinrich Layer 1 and its role in the last deglaciation. Paleoceanography 32, 284-303.

Hopmans, E.C., Schouten, S., Sinninghe Damsté, J.S., 2015. The effect of improved chromatography on GDGT-based palaeoproxies, Organic Geochemistry. doi: http://dx.doi.org/10.1016/j.orggeochem.2015.12.006.

Hopmans, E.C., Weijers, J.W., Schefuß, E., Herfort, L., Damsté, J.S.S., Schouten, S., 2004. A novel proxy for terrestrial organic matter in sediments based on branched and isoprenoid tetraether lipids. *Earth and Planetary Science Letters, 224*(1-2), 107-116.

Huck, C.E., van de Flierdt, T., Bohaty, S.M., Hammond, S.J., 2017. Antarctic climate, Southern Ocean circulation patterns, and deep water formation during the Eocene, Paleoceanography, 32, 674–691. doi: 10.1002/2017PA003135.

IPCC: Climate Change 2013: The Physical Science Basis, Contribution of Working Group I to the Fifth Assessment Report of the Intergovernmental Panel on Climate Change, Cambridge University Press, Cambridge, United Kingdom and New York, NY, USA, 2013.

Jacobsen, S.B., Wasserburg, G. 1980. Sm-Nd isotopic evolution of chondrites, *Earth and Planetary Science Letters*, *50*(1), 139-155.

Jimenez-Espejo, F.J., Martinez-Ruiz, F., Sakamoto, T., Iijima, K., Gallego-Torres, D., Harada, N.: Paleoenvironmental changes in the western Mediterranean since the last glacial maximum: High resolution multiproxy record from the Algero-Balearic basin. Palaeogeogr. Palaeoclimatol. Palaeoecol., 246, 292–306, doi:10.1016/j.palaeo.2006.10.005, 2007.

Jovane, L., Florindo, F., Acton, G., Ohneiser, C., Sagnotti, L., Strada, E., Verosub, K. L., Wilson, G. S., Iacoviello, F., Levy, R. H., Passchier, S., 2019. Miocene glacial dynamics recorded by variations in magnetic properties in the ADRILL-2A drill core. American Geophysical Union, doi: 10.1029/2018JB016865

Kim, J.H., Van der Meer, J., Schouten, S., Helmke, P., Willmott, V., Sangiorgi, F., Koç, H., Hopmans, E.C., Sinninghe Damsté, J. S, 2010. New indices and calibrations derived from the distribution of crenarchaeal isoprenoid tetraether lipids: Implications for past sea surface temperature reconstructions. *Geochimica et Cosmochimica Acta*, *74*(16), 4639-4654.

Kulhanek, D., Levy, R., Clowes, C.D., Prebble, J.G., Rodelli, D., Jovane, L., Morgans, H.E.G., Kraus, C., Zwingmann, H., Griffith, E.M., Scher, H.D., McKay, R.M., Naish, T.R. 2019. Revised chronostratigraphy of DSDP Site 270 and late Oligocene to early Miocene paleoecology of the Ross Sea sector of Antarctica, Global and Planetary Change, 178, 46-64.

Lambelet, M., van de Flierdt, T., Butler, E.C.V., Bowie, A.R., Rintoul, S.R., Watson, R.J., Remenyi, T., Lannuzel, D., Warner, M., Robinson, L.F., Bostock, H.C. Bradtmiller, L.I, 2018. The neodymium isotope fingerprint of Adélie Coast Bottom Water. Geophysical Research Letters, 45, 11,247–11,256. https://doi. org/10.1029/2018GL080074.

Levy, R.H., Meyers, S.R., Naish, T.R.,Golledge, N.R., McKay, R.M., Crampton, J.S., DeConto, R.M., De Santis, L., Florindo, F., Gasson, E.G.W., Harwood, D.M., Luyendyk, B.P., Powell, R.D., Clowes, C., Kulhanek, D.K. 2019. Antarctic ice-sheet sensitivity to obliquity forcing enhanced through ocean connections. Nature Geosciences 12, 132-137.

Liebrand, D., De Bakker, A.T.M., Beddow, H.M., Wilson, P.A., Bohaty, S.M., Ruessink, G., Pälike, H., Batenburg, S.J., Hilgen, F.J., Hodell, D.A., Huck, C.E., Kroon, D., Raffi, I., Saes, M.JM., van Dijk, A.E., Lourens, L., 2017. "Evolution of the Early Antarctic Ice Ages" 114 (15): 3867–72. https://doi.org/10.1073/pnas.1615440114.

Liu, Y., Moore, J.C., Cheng, X., Gladstone, R M., Bassis, J.N., Liu, H., Wen, J., Hui, F., 2015. Ocean-driven thinning enhances iceberg calving and retreat of Antarctic ice shelves, P. Natl. Acad. Sci. USA, 112, 3263–3268. https://doi.org/10.1073/pnas.1415137112.

Lyle, M., Gibbs, S., C. Moore, T.C., Rea, D.K., 2007. Late Oligocene Initiation of the Antarctic Circumpolar Current: Evidence from the South Pacific. *Geology* 35 (8): 691–94. https://doi.org/10.1130/G23806A.1.

Martini, E., 1971. Standard Tertiary and Quaternary calcareous nannoplanktonzonation. In: Farinacci, A. (Ed.), Proceeding II Plankt. Conf., Roma, 1970, vol. 2,pp. 739–785.

Martin, E.E., Scher, H.D., 2004. Preservation of seawater Sr and Nd isotopes in fossil fish teeth: bad news and good news, Earth Planet. Sci. Lett. 220, 25–39.

Martin, E.E., Scher, H.D., 2006. A Nd isotopic study of southern sourced waters and Indonesian Throughflow at intermediate depths in the Cenozoic Indian Ocean, Geochemistry, Geophysics, Geosystems, 7(9). doi: 10.1029/2006GC001302

Meredith, M., M. Sommerkorn, M., Cassotta, S., Derksen, C., Ekaykin, A., Hollowed, A., Kofinas, G., Mackintosh, A., Melbourne- Thomas, J., Muelbert, M.M.C., Ottersen, G., Pritchard, H., and Schuur, E.A.G. 2019: Polar Regions. In: IPCC Special Report on the Ocean and Cryosphere in a Changing Climate).

Moiroud, M., Pucéat, E., Donnadieu, Y., Bayon, G., Moriya, K., Deconinck, J-F., Boyet, M., 2013. Evolution of the neodymium isotopic signature of neritic seawater on a northwestern Pacific margin: New constrains on possible end-members for the composition of deep-water masses in the Late Cretaceous ocean, Chem. Geol., 356, 160–170. http://dx.doi.org/10.1016/j.chemgeo.2013.08.008.

Müller, R.D., Cannon, J., Qin, X., Watson, R.J., Gurnis, M., Williams, S., et al., 2018. GPlates: Building a virtual Earth through deep time. Geochemistry, Geophysics, Geosystems, 19. doi:10.1029/2018GC007584.

Naish, T.R., Wilson, G.S., Dunbar, G.B., Barrett, P.J., 2008. Constraining the amplitude of Late Oligocene bathymetric changes in western Ross Sea during orbitally-induced oscillations in the East Antarctic Ice Sheet: (2) implications or global sea-level changes. Palaeogeogr. Palaeoclimatol. Palaeoecol. 260, 66–76. doi:10.1016/j.palaeo.2007.08.021.

Nakayama, Y., Menemenlis, D., Zhang, H., Schodlok, M., Rignot, E., 2018. Origin of Circumpolar Deep Water Intruding onto the Amundsen and Bellingshausen Sea Continental Shelves. *Nature Communications* 9 (1): 1–9. https://doi.org/10.1038/s41467-018-05813-1.

Nelson, C.S., Cooke, P.J., 2001. History of Oceanic Front Development in the New Zealand Sector of the Southern Ocean during the Cenozoic—a Synthesis. *New Zealand Journal of Geology and Geophysics* 44 (4): 535–53. https://doi.org/10.1080/00288306.2001.9514954.

Lucchi, R.G, Rebesco, M., 2007. Glacial contourites on the Antarctic Peninsula margin: insights for palaeoenvironmental and paleoclimatic conditions. Geol. Soc. Spec. Publi., 276, 111-127. https://doi.org/10.1144/GSL.SP.2007.276.01.06.

Olbers, D., Borowski, D., Völker, C., Wölff, J., 2004. The dynamical balance, transport and circulation of the Antarctic Circumpolar Current, Antarct. Sci., 16, 439–470.

Orsi, A.H., Whitworth, T., Nowlin, W.D., 1995. On the meridional extent and fronts of the Antarctic Circumpolar Current, Deep-Sea Res. Pt. I, 42, 641–673. https://doi.org/10.1016/0967-0637(95)00021-W.

Passchier, S., Ciarletta, D.J., Henao, V., Sekkas, V., 2018. Sedimentary processes and facies on a high-latitude passive continental margin, Wilkes Land, East Antarctica. Geological Society, London Special Publications, 475, 181-201. http://doi.org/10.6084/m9.figshare.c.4031218.v1.

Patterson, M.O., McKay, R., Naish, T., Escutia, C., Jimenez- Espejo, F.J., Raymo, M.E., Meyers, S.R., Tauxe, L., Brinkhuis, H., Klaus, A., Fehr, A., Bendle, J.A.P., Bijl, P.K., Bohaty, S.M., Carr, S. A., Dunbar, R.B., Flores, J.A., Gonzalez, J.J., Hayden, T.G., Iwai, M., Katsuki, K., Kong, G.S., Nakai, M., Olney, M.P., Passchier, S., Pekar, S.F., Pross, J., Riesselman, C.R., Röhl, U., Sakai, T., Shrivastava, P.K., Stickley, C.E., Sugasaki, S., Tuo, S., van de Flierdt, T., Welsh, K., Williams, T., Yamane, M., 2014. Orbital forcing of the East Antarctic ice sheet during the Pliocene and Early Pleistocene, Nat. Geosci., 7, 841 847. https://doi.org/10.1038/ngeo2273, 2014.

Pekar, S.F., DeConto, R.M., Harwood, D.M., 2006. Resolving a late Oligocene conundrum: Deep-sea warming and Antarctic glaciation, Palaeogeogr. Palaeocl., 231, 29–40.

Pekar, S.F., Christie-Blick, N., 2008. Resolving Apparent Conflicts between Oceanographic and Antarctic Climate Records and Evidence for a Decrease in p CO 2 during the Oligocene through Early Miocene (34 – 16 Ma), 260: 41–49. https://doi.org/10.1016/j.palaeo.2007.08.019.

Pfuhl, H.A., McCave, I.N., 2005. Evidence for Late Oligocene Establishment of the Antarctic Circumpolar Current. *Earth and Planetary Science Letters* 235 (3–4): 715–28. https://doi.org/10.1016/j.epsl.2005.04.025.

Piper., D.J.W., Brisco, C., 1975. Deep-water continental-margin sedimentation , dsdp Leg 28, Antarctica. *In* Hayes D:E., Frakes, L.A., et al., 1975 Initial Reports of the Deep Sea Drilling Project, Vol. 28, U.S. Government Printing Office, Washington pp.727-755. doi:10.2973/dsdp.proc.28.121.1975.

Prebble, J., Crouch, E., Carter, L., Cortese, G., Bostock, H., Neil, H., 2013. An expanded modern dinoflagellate cyst dataset for the Southwest Pacific and Southern Hemisphere with environmental associations. *Marine Micropaleontology, 101*, 33-48.

Pritchard, H.D., Ligtenberg, S.R. M., Fricker, H.A., Vaughan, D.G., Van Den Broeke, M.R., Padman, L., 2012. Antarctic Ice-Sheet Loss Driven by Basal Melting of Ice Shelves." *Nature* 484 (7395): 502–5. https://doi.org/10.1038/nature10968.

Rebesco, M., Hernández-Molina, F.J., Van Rooij, D., Wåhlin, A., 2014. Contourites and associated sediments controlled by deep-water circulation processes: State-of-theart and future considerations, Mar. Geol., 352, 111–154. https://doi.org/10.1016/j.margeo.2014.03.011.

Richey, J.N., Tierney, J.E., 2016. GDGT and alkenone flux in the northern Gulf of Mexico: Implications for the TEX86 and UK'37 paleothermometers. *Paleoceanography, 31*(12), 1547-1561.

Rignot, E., Mouginot, J., Scheuchl, B., van den Broeke, M., van Wessem., M., Morlighem, M., 2019. Four decades of Antarctic Ice Sheet mass balance from 1979–2017.

Rintoul, S.R., 1998. On the origin and influence of Adélie Land Bottom Water. In Ocean, ice, and atmosphere: Interactions at the Antarctic continental margin (Vol. 75, pp. 151–171). Washington, DC: American Geophysical Union.

Rintoul, S. R., 2018. The global influence of localized dynamics in the Southern Ocean. Nature, 558 (7709), 209–218. https://doi.org/10.1038/s41586-018-0182-3

Rintoul, S.R., Hughes, C., Olbers, D., 2001. The Antarctic circumpolar current system. In G. Siedler, J. Church, J. Gould (Eds.), Ocean circulation and climate. New York: Academic Press. Proc. Natl. Acad. Sci. USA, pp. 271-302.

Rodriguez-Tovar, F.J., Dorador, J., 2014. Ichnological analysis of pleistocene sediments from the IODP Site U1385 “Shackleton Site” on the Iberian margin: approaching paleoenvironmental conditions. Palaeogeogr. Palaeoclimatol. Palaeoecol. 409,24–32.

Rodríguez-Tovar, F.J., Dorador, J., 2015. Ichnofabric characterization in cores: a method of digital image treatment. Ann. Soc. Geol. Pol. 85 (3), 465–471.

Rodríguez-Tovar, F.J., Nagy, J., Reolid, M., 2014. Palaeoenvironment of Eocene prodelta in Spitsbergen recorded by the trace fossil Phycosiphon incertum. Polar Res. 33, 23786.

Rodríguez-Tovar, F.J., Dorador, J., Martin-Garcia, G.M., Sierro, F.J., Flores, J.A., Hodell, D.A., 2015a. Response of macrobenthic and foraminifer communities to changes in deep-sea environmental conditions from marine isotope stage (MIS) 12 to 11 at the “Shackleton Site”. Glob. Planet. Chang. 133, 176–187.

Rodríguez-Tovar, F.J., Dorador, J., Grunert, P., Hodell, D., 2015b. Deep-sea trace fossil and benthic foraminiferal assemblages across glacial terminations 1, 2 and 4 at the “Shackleton Site” (IODP Expedition 339, Site U1385). Glob. Planet. Chang. 133, 359–370.

Rodríguez-Tovar, F.J., Dorador, J., Hodell, D.A.V. 2019. Trace fossils evidence of a complex history availability and oxygen conditions during Heinrich Event 1. Global and Planetary Change, 174, 26-34.

Salabarnada, A., Escutia, C., Röhl, U., Nelson, C.H., McKay, R., Jiménez-Espejo, F.J., Bijl, P. K., Hartman, J.D., Strother, S. L., Salzmann, U., Evangelinos, D., López-Quirós, A., Flores, J.A., Sangiorgi, F., Ikehara, M., Brinkhuis, H., 2018. Paleoceanography and ice sheet variability offshore Wilkes Land, Antarctica – Part 1: Insights from late Oligocene astronomically paced contourite sedimentation, Clim. Past, 14, 991–1014, https://doi.org/10.5194/cp-14-991-2018.

Sangiorgi, F., Bijl, P.K., Passchier, S., Salzmann, U., Schouten, S., McKay, R., Cody, R. D., Pross, J., Van De Flierdt, T., Bohaty, S. M., Levy, R., Williams, T., Escutia, C., Brinkhuis, H., 2018. Southern Ocean warming and Wilkes Land ice sheet retreat during the mid-Miocene, Nat. Commun., 9, 317, https://doi.org/10.1038/s41467-017-02609-7.

Scher, H.D., Bohaty, S.M., Zachos, J. C., Delaney, M.L., 2011. Two-stepping into the icehouse: East Antarctic weathering during progressive ice-sheet expansion at the Eocene–Oligocene transition. Geology 39, 383–386.

Scher, H.D., Martin, E.E., 2004. Circulation in the Southern Ocean during the Paleogene inferred from neodymium isotopes. Earth Planet. Sci. Lett. 228, 391–405.

Schouten, S., Hopmans, E.C., Rosell-Melé, A., Pearson, A., Adam, P., Bauersachs, T., Brocks, J.J., et al., 2013. An interlaboratory study of TEX86 and BIT analysis of sediments, extracts, and standard mixtures. *Geochemistry, Geophysics, Geosystems, 14*(12), 5263-5285.

Schouten, S., Hopmans, E.C., Schefuß, E., Damste, J.S.S., 2002. Distributional variations in marine crenarchaeotal membrane lipids: a new tool for reconstructing ancient sea water temperatures? *Earth and Planetary Science Letters, 204*(1-2), 265-274.

Scotese, C.R., Wright, N., 2018. PALEOMAP Paleodigital Elevation Models (PaleoDEMS) for the Phanerozoic PALEOMAP Project, https://www.earthbyte.org/paleodem-resource-scotese-and-wright-2018.

Seki, A., Tada, R., Kurokawa, S., Murayama, M., 2019. High-resolution Quaternary record of marine organic carbon content in the hemipelagic sediments of the Japan Sea from bromine counts measured by XRF core scanner *Progress in Earth and Planetary Science* volume 6, Article number: 1 (2019).

Seton, M., Müller, R.D., Zahirovic, S., Gaina, C., Torsvik, T.H., Shephard, G., Talsma, A., Gurnis, M., Turner, M., Maus, S., Chandler, M., 2012. Global continental and ocean basin reconstructions since 200 Ma, Earth-Science Reviews, Volume 113, Issues 3-4, July 2012, Pages 212-270, ISSN 00128252,10.1016/j.earscirev.2012.03.002.

Shanmugam, G., Spalding, T.D., Rofheart, D.H.,1993. Traction structures in deep-marine, bottom-current-reworked sands in the Pliocene and Pleistocene, Gulf of Mexico, Geology, 21, 929–932. https://doi.org/10.1130/0091-7613(1993)021<0929:TSIDMB>2.3.CO;2.

Shaw, H., Wasserburg, G., 1985. Sm-Nd in marine carbonates and phosphates: Implications for Nd isotopes in seawater and crustal ages, Geochimica et Cosmochimica Acta, 49(2), 503-518.

Sluijs, A., Pross, J., Brinkhuis, H., 2005. From greenhouse to icehouse; organic-walled dinoflagellate cysts as paleoenvironmental indicators in the Paleogene. *Earth-Science Reviews, 68*(3-4), 281-315.

Sokolov, S., Rintoul, S.R., 2002. Structure of Southern Ocean fronts at 140_{o}E, J. Mar. Syst., 37, 151– 184. doi:10.1016/S0924-7963(02)00200-2.

Sokolov, S., Rintoul, S.R., 2009. Circumpolar structure and distribution of the Antarctiv Circumpolar Current fronts: 1. Mean circumpolar paths. J. Geophysical Research, 14, doi:10.1029/2008JC005108.

Sorlien, C.C., Luyendyk, B.P., Wilson, D.S., Bartek, L.R., Diebold, J.B., 2007. Oligocene development of the West Antarctic Ice Sheet recorded in eastern Ross Sea strata. Geology 35, 467–470.

Stow, D., Faugères, J.-C., 2008. Contourite Facies and the Facies Model, chap. 13, 223–256.

Tachikawa, K.,V. Athias, C. Jeandel, 2003. Neodymium budget in the modern ocean and paleo-oceanographic implications, Journal of Geophysical Research: Oceans (1978–2012), 108(C8).

Tanaka, T., Togashi, S., Kamioka, H., Amakawa, H., Kagami, H., Hamamoto, T., Yuhara, M., Orihashi, Y., Yoneda, S., Shimizu, H., Kunimaru, T., Takahashi, K., Yanagi, T., Nakano, T., Fujimaki, H., Shinjo, R., Asahara, Y., Tanimizu, M., Dragusanu, C., 2000. JNdi-1: a neodymium isotopic reference in consistency with LaJolla neodymium. Chemical Geology, 168, 279-281.

Taylor, K.W., Huber, M., Hollis, C.J., Hernandez-Sanchez, M.T., Pancost, R.D., 2013. Re-evaluating modern and Palaeogene GDGT distributions: Implications for SST reconstructions. *Global and Planetary Change, 108*, 158-174.

Thompson, D.W.J., Solomon, S., 2002. Interpretation of recent Southern Hemisphere climate change. Science 296, 895–899.

Toggweiler, J. R., Russell, J., 2008. Ocean circulation in a warming climate, Nature, 451, 286–288. https://doi.org/10.1038/nature06590.

van de Flierdt, T., Griffiths, A.M., Lambelet, M., Little, S.H., Stichel, T., Wilson, D., 2016. Neodymium in the oceans: a global database, a regional comparison and implications for palaeoceanographic research. Philos. Trans. R. Soc. A 374, 20150293.

van Wijk, E.M., Rintoul, S.R., 2014. Freshening drives contraction of Antarctic Bottom Water in the Australian Antarctic Basin, Geophys. Res. Lett., 41, 1657–1664. https://doi.org/10.1002/2013GL058921.

Weis, D., Kieffer, B., Maerschalk, C., Barling J., de Jong, J., Williams, G.A., Hanano, D., Pretorius, W., Mattielli, N., Scoates, J.S., 2006. High-precision isotopic characterization of USGS reference materials by TIMS and MC-ICP-MS, Geochemistry, Geophysics, Geosystems, 7(8), Q08006.

Whitehead, J.M., Bohaty, S.M., 2003. Pliocene summer sea surface temperature reconstruction using silicoflagellates from Southern Ocean ODP Site 1165, Paleoceanography, 18. https://doi.org/10.1029/2002PA000829.

Wilson D.J., Piotrowski, A.M., Galy, A., Clegg, J.A., 2013 Reactivity of neodymium carriers in deep sea sediments: implications for boundary exchange and paleoceanography. Geochim. Cosmochim. Acta 109, 197–221. doi:10.1016/j.gca.2013.01.042.

Wright, N., Scher, H.D., Seton, M., Huck, C.E., Duggan, B.D., 2018.No Change in Southern Ocean Circulation in the Indian Ocean From the Eocene Through Late Oligocene', Paleoceanography and Paleoclimatology, 33(2), pp. 152–167. doi: 10.1002/2017PA003238.

Zachos, J., Pagani, M., Sloan, L., Thomas, E., Billups, K., 2001. Trends, rhythms, and aberrations in global climate 65 Ma to present, Science, 292, pp. 686–693.

Zhang, Y.G., Pagani, M., Liu, Z., Bohaty, S. M., Deconto, R., 2013. A 40-million-year history of atmospheric CO2, Philos. T. R. Soc. A, 371, 20130096. https://doi.org/10.1098/rsta.2013.0096.

Zhang, Y.G., Pagani, M., Wang, Z., 2016. Ring Index: A new strategy to evaluate the integrity of TEX86 paleothermometry. *Paleoceanography*, *31*(2), 220-232.

Zhang, Y. G., Zhang, C. L., Liu, X.-L., Li, L., Hinrichs, K.-U., Noakes, J. E., 2011. Methane Index: A tetraether archaeal lipid biomarker indicator for detecting the instability of marine gas hydrates. *Earth and Planetary Science Letters, 307*(3-4), 525-534.

Zonneveld, K.A., Marret, F., Versteegh, G.J., Bogus, K., Bonnet, S., Bouimetarhan, I., Crouch, E., de Vernal, A., Elshanawany, R., Edwards, L., Esper, O., Forke, S., Grøsfjeld, K., Henry, M., Holzwarth, U., Kielt, J.F., Y., Kim, S.Y., Ladouceur, S., Ledu, D., Chen, L.,. Limoges, A., Londeix, L., Lu, S.H., Mahmoud, M.S., Marino, G., Matsouka, K., Matthiessen, J., Mildenhal, D., Mudie, P., Neil, H., Pospelova, V.,. Qi, Y., Radi, T., Richerol, T., Rochon, A., Sangiorgi, F., Solignac, S., Turon, J.L., Verleye, T., Wang, Y., Wang, Z., Young M., 2013. Atlas of modern dinoflagellate cyst distribution based on 2405 data points. *Review of Palaeobotany and Palynology*, *191*, 1-197. https://doi.org/10.1016/j.revpalbo.2012.08.003.

List of Figures

Figure 1. Oceanic frontal system between Antarctica and Australia**.** Dark Blue dashed lines schematically represent oceanic fronts today (Sokolov and Rintoul, 2009). Polar water south of the PF are shaded in darker blue. Map derived from Gplates software (Müller et al., 2018). Site 269 is marked with yellow symbol and Site U1356 is marked with red symbol. White lines indicates the continental lithosphere boundary. Black arrows show the pathway of the ACC today (Rintoul et al., 2001). STF: Subtropical front, SAF: Subantarctic front, PF: Polar Front, SAACF: Southern ACC front, ACC: Antarctic Circumpolar Current.

Figure 2. Age model for Deep Sea Drilling Project Hole 269A based on magnetostratigraphy constrained by dinocyst and calcareous nannofossil biostratigraphy. **LO:** Last Occurrence. **P:** Presence. Age model has been calibrated to GTS2012 of Gradstein et al. (2012).

Figure 3. Sedimentological, paleontological and geochemical (XRF scanning data and $\varepsilon_{Nd(t)}$) data of DSDP Hole 269A, all plotted versus depth **a:** Graphic lithological log, **b:** sedimentary structures (see legend), **c:** main facies distribution (see legend), **d:** total Ca counts, **e:** total Ti counts, **f:** Zr/Ti ratios, **g:** Br/Ti ratios, **h:** ε_{Nd}, **i:** TEX_{86}-derived sea surface temperature **k:** %P-cyst=P-cyst/(P-cyst + G-cyst).Colors of TEX_{86}-derived SST and P-cyst vs G-cyst values reflect the sedimentary facies. Note core gaps between the cores were removed from the plot (gaps indicated with //).

Figure 4. Representative core photographs from facies assemblages in DSDP Hole 269A, showing main structures and bed contacts referred to in the text. Facies colour code in the sidebar to the right of each core image is according to the legend in Figure 3. ft: faint

laminations, pl: planar laminations, wa: wavy laminations, *dm:* double mud layers, rp: ripple, cr: cross-laminations, mo: mud-offshoots, sd: soft-sedimentary structures, m: mottled, *Ch: Chondrites, Pl: Planolites, Th: Thalassinoides, Scolicia: Sc.* Note single granule in core photos: g and k. Numbers below core photos show core section and depth (mbsf).

Figure 5. Detailed images of carbonate-cemented facies. **a**: A sharp erosive contact (sc-e) between bioturbated (F3b) and laminated (F3a) carbonate-cemented facies. **b, c, d:** A carbonate-cemented bioturbated and laminated facies. **e:** Back-scattered electron photomicrograph showing blow-up example of a sharp erosive contact (sc-e) between bioturbated and laminated carbonate-cemented facies (red dotted line) and inverse grading pattern (yellow arrow) above the contact . **f:** Thin section photomicrograph, plain-polarized light of carbonate-cemented facies showing diatom assemblages within the laminae of facies F3a. **g:** HR-SEM micrograph and corresponding elemental map of Al, Ca, Si showing diatom skeletal remains within the carbonate cementation matrix. **h:** foraminifera with siliceous tests. *Ch: Chondrites*, *Pl: Planolites, Th: Thalassinoides,* pl: planar laminations, rp: ripple, cr: cross-laminations.

Figure 6. Principal Component Analysis (PCA) between XRF-scanner data through the study core section. **a:** $PC1_{TOT}$ with carbonate-cemented facies and **b:** PC1 without carbonate-cemented facies.

Figure 7. Paleoceanographic configuration offshore the Wilkes Land margin around 24-23 Ma. **a:** Reconstructed ocean frontal system between Antarctica and Australia around 24-23 Ma. Reconstruction of tectonic plates around Tasman Gateway and paleoposition of sites based on

Seton et al., 2012 global plate motion model derived from Gplates software (Müller et al., 2018). White lines indicate the continental lithosphere boundary. Polar water south of the PF are shaded in darker blue. Boundary between polar and subantarctic waters during the 23.23 Ma (red dashed line) and during the 24 Ma (yellow dashed line). Frontal constraints west and east of the Wilkes Land region are from reconstructions of Nelson and Cooke (2001); Cooke et al. (2002). STF: Subtropical front, SAF Subantarctic front, PF: Polar front. Black arrows show the pathway of the proto-ACC. Schematic illustrations of proto-CDW dynamics for the 24 Ma (b) and 23.23 Ma (c). **b:** At ~ 24 Ma, Westerlies and PF were located close to Site 269 resulting strong proto-ACC. There is likely enhanced proto-AABW production. **c:** At ~ 23.23 Ma, Westerlies and PF migrated southwards close to Site U1356. Proto-ABBW formation is reduced. This allowed the relative warmer surface water and proto-CDW to penetrate closer to Antarctic continent.

Figures

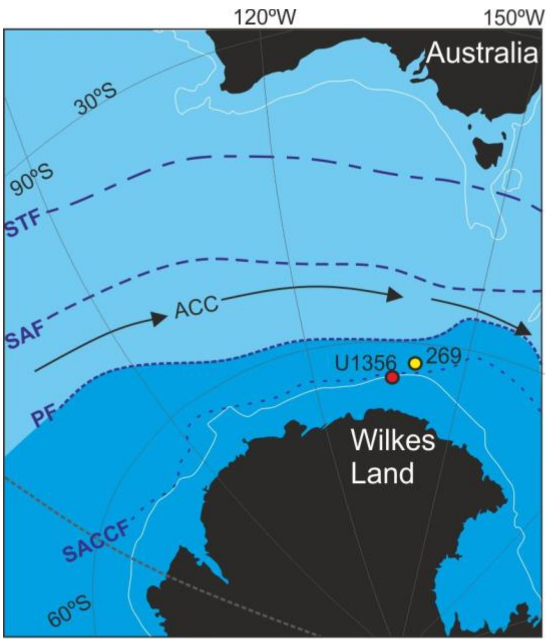

Figure 1- in colour

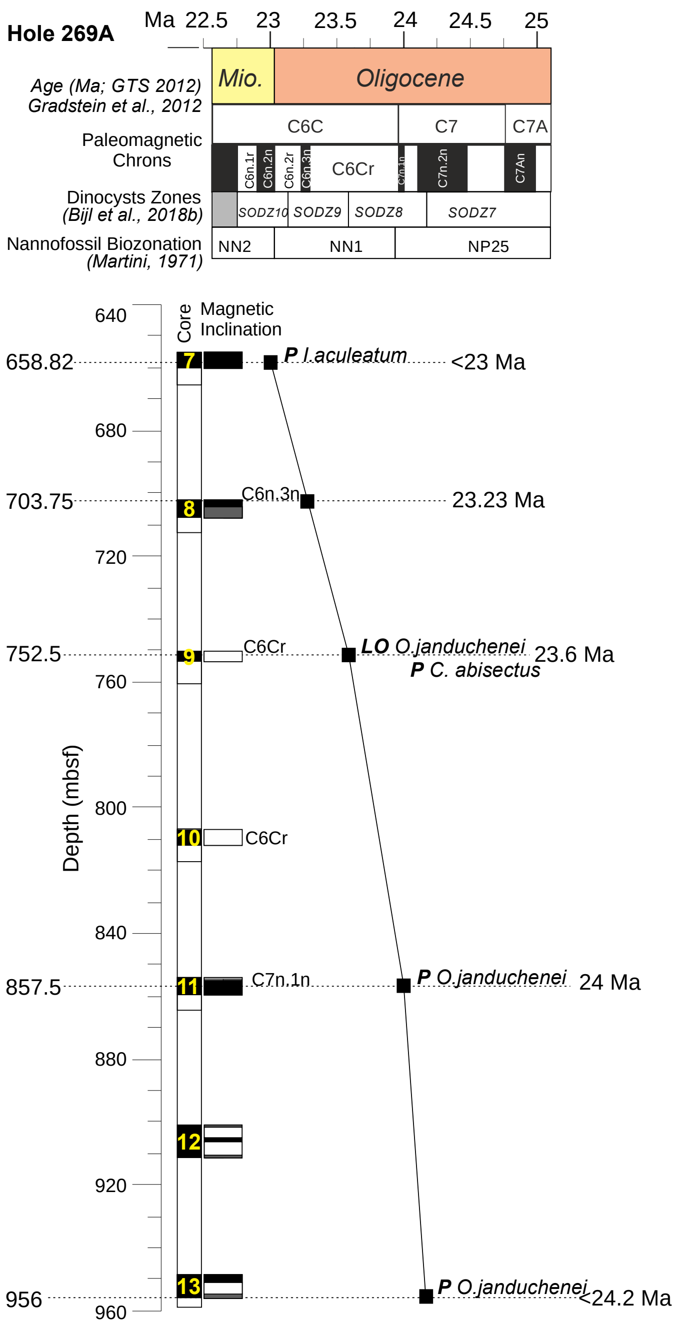

Figure 2- in colour

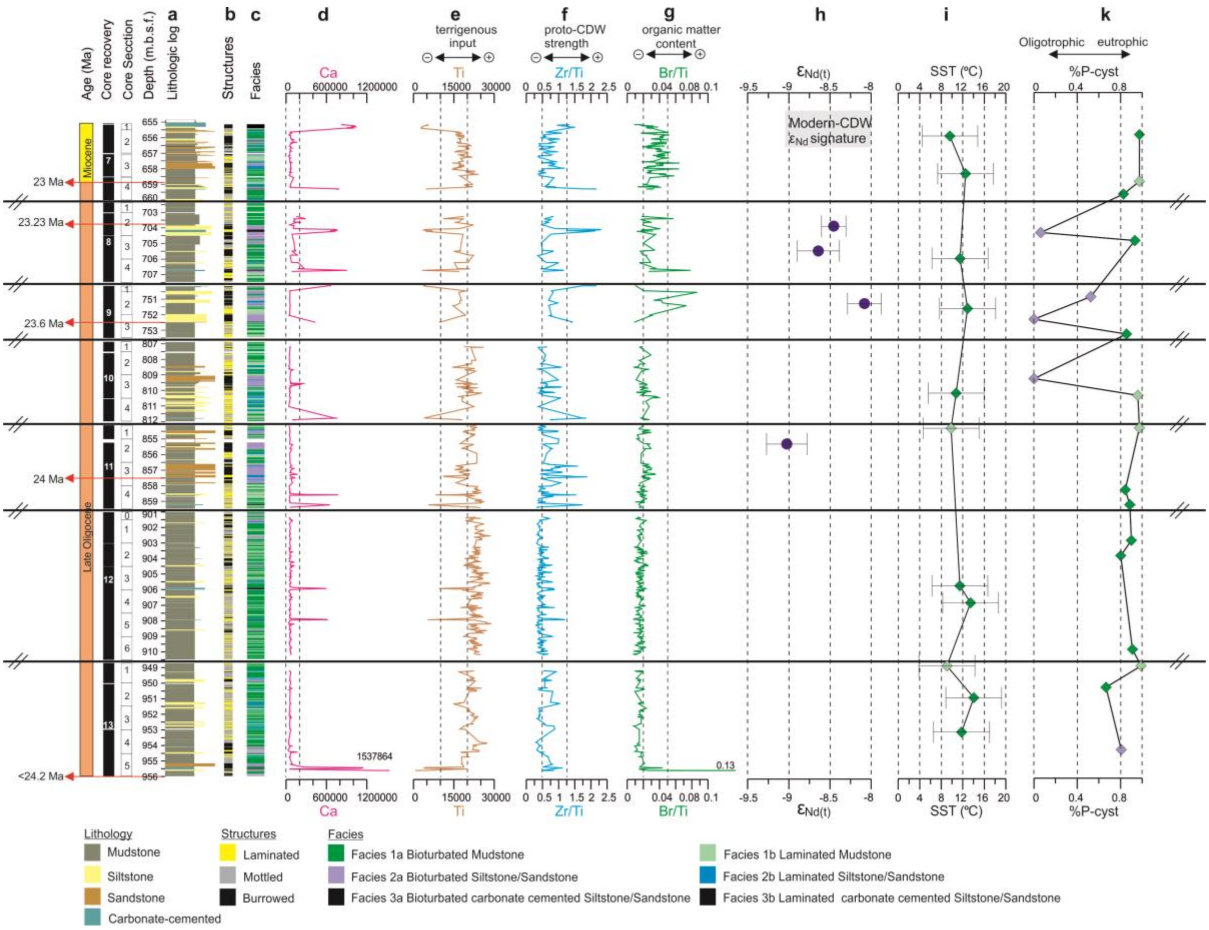

Figure 3- in colour

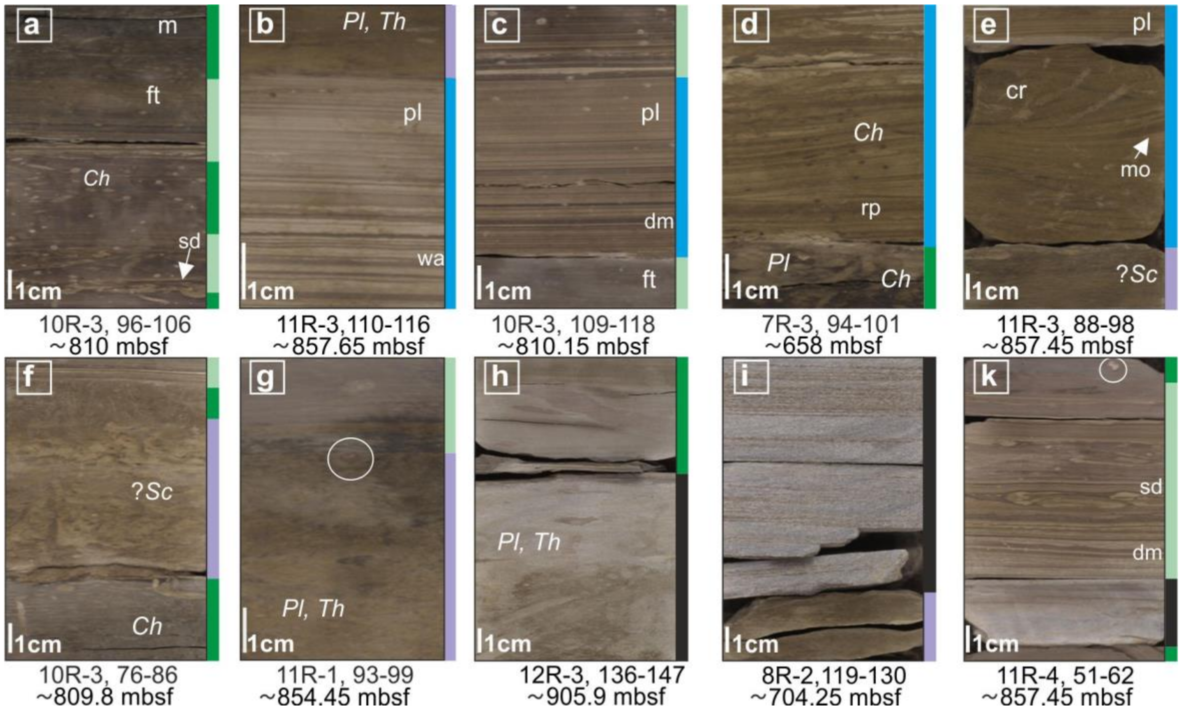

Figure 4- in colour

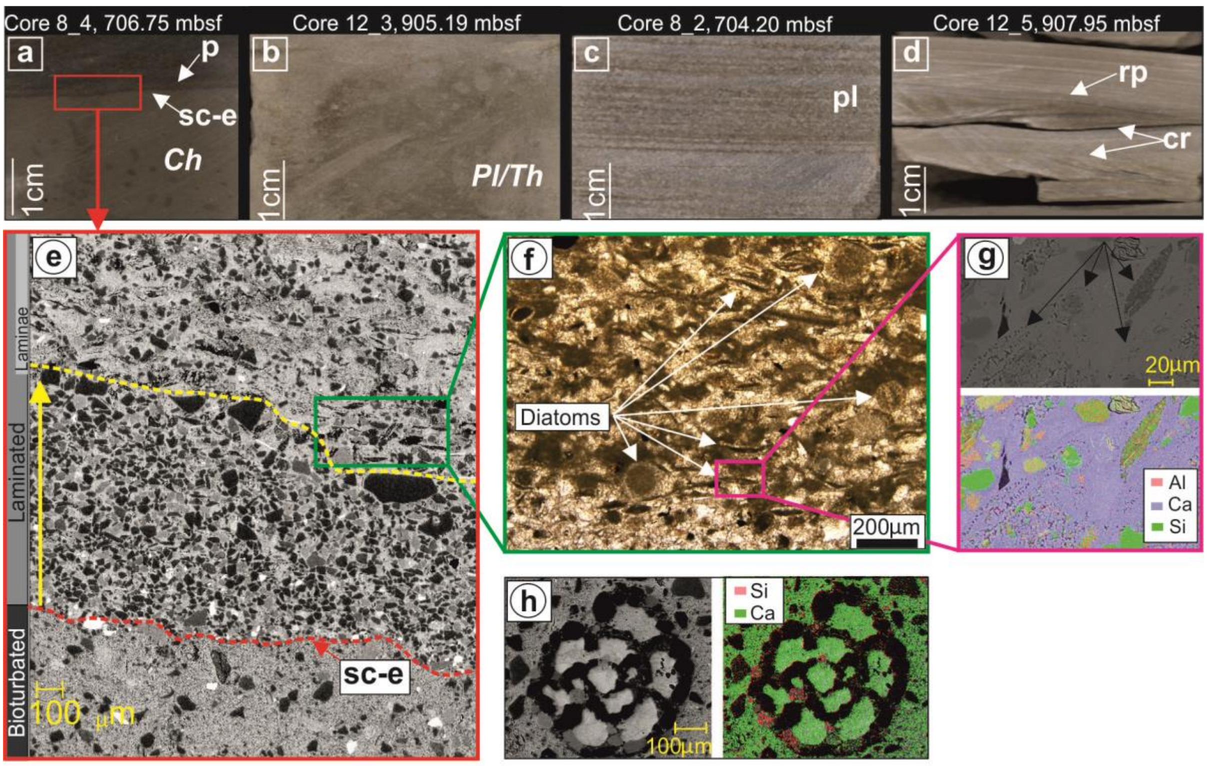

Figure 5-in colour

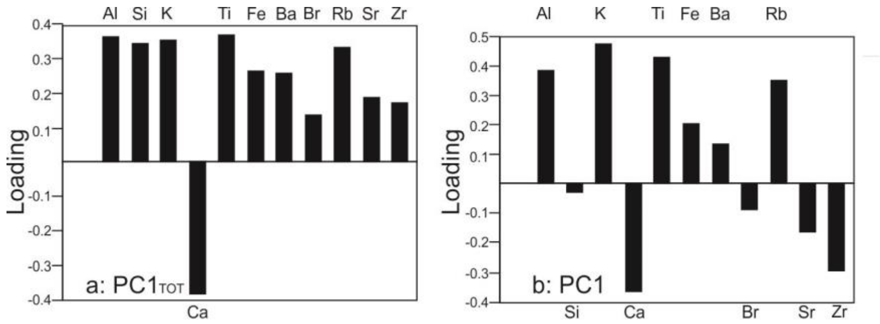

Figure 6-black and white

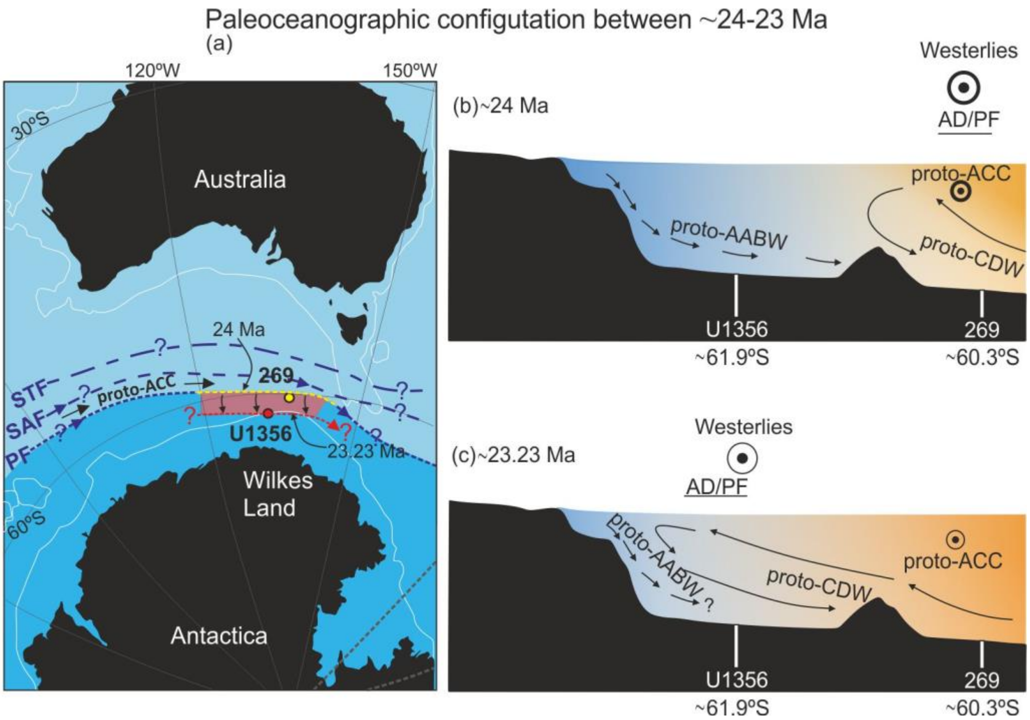

Figure 7-in colour

Supplementary Material

Supplementary text

Fossil fish tooth sample preparation for Neodymium isotopes

Fish debris was handpicked from the >63 μm sediment fractions that were prepared by wet sieving. Four samples were prepared for fish-tooth and bone debris Nd isotope analyses. All samples were treated with ultraclean 18 MΩ water (MQ water) and methanol-following Martin and Haley (2000) to remove debris from surfaces and cavities in the MAGIC laboratories at Imperial College London (see also Huck et al., 2017). Cleaned fish tooth samples were subsequently transferred into cleaned microcentrifuge tubes and dissolved overnight in 50 μL of 2M HCl. Dissolved fish debris were loaded on Biorad cation exchange resin (200-400 μm mesh) to separate the REEs from the sample matrix and Eichrom Ln-Spec resin (50-100 μm bead size) to separate Nd from the other REEs.

Bulk sediment sample preparation for Neodymium isotopes

In order to consider a potential influence of the detrital sediment towards the Nd isotope composition of pore waters or overlying bottom water, we also measured the Nd isotope compositions of two detrital sediment samples. Samples were dried and gently homogenised using mortar and pestle. Approximately 500 mg of homogenised material was subjected to a carbonate leaching procedure to remove biogenic carbonate using 30 ml of 1.5% buffered acetic acid (see Biscaye (1965) for more details). Ferromanganese oxides and oxyhydroxides were leached using a weak reductive solution of 0.005 M Hydroxylamine Hydrochloride (NH_2OH), followed by a stronger solution of 0.05 M NH_2OH. 50 mg of leached detrital sediment sample was subsequently digested on a hotplate using a mixture of 1ml of concentrated HNO_3, 0.8ml $HClO_4$ and 2 ml HF. The detrital samples were processed using the same ion chromatography as the fish debris.

Supplementary figures

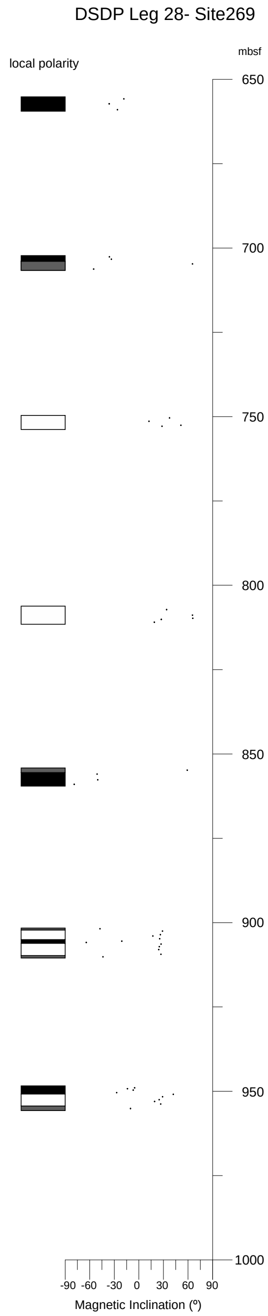

Figure S1. Stratigraphic location of the calculated Inclinations for the Site 269. A local polarity, where negative (positive) inclinations indicate normal (reversed) polarity in black (white), is also provided. Magnetozones are defined by more than one sample, otherwise they are shown in grey.

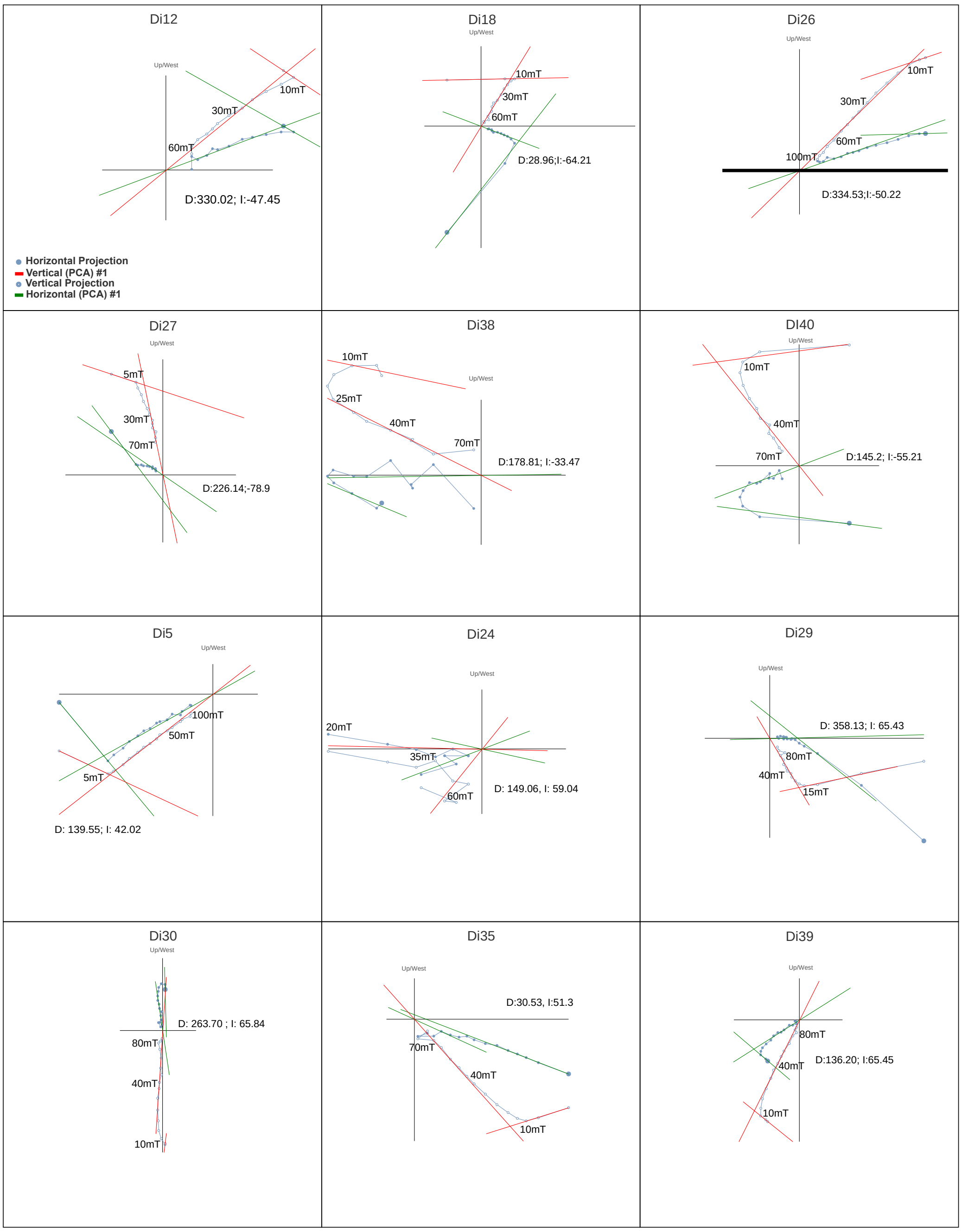

Figure S2. Orthogonal plots of the representative samples, showing two distinctive directions, both in normal samples and in reversed samples. Inclination values are also indicated. Open plots indicate inclinations (vertical projection). All calculated directions are available in Table S1. Samples were calculated by means of the Paldir and paleomagnetism.org (Koymans et al., 2016) programs.

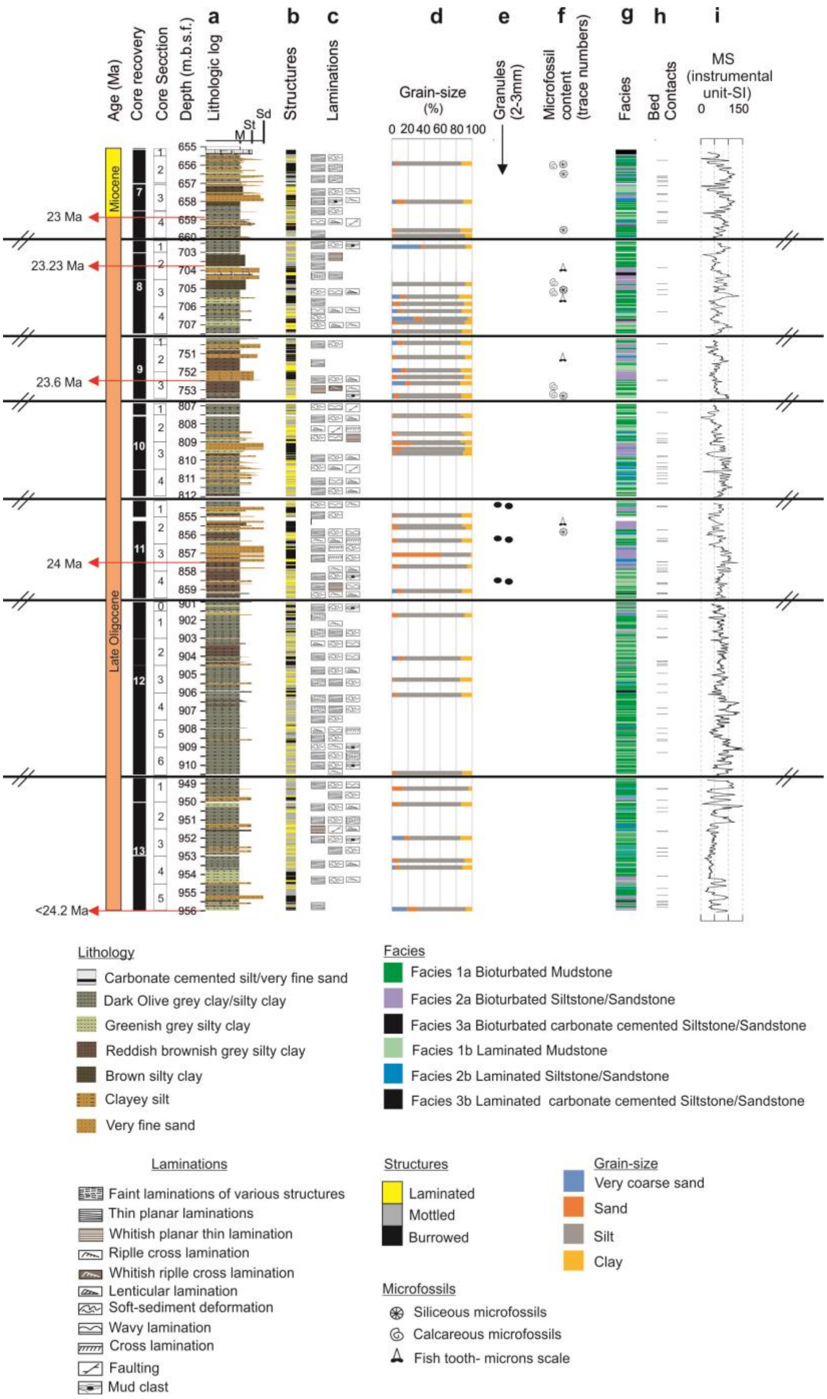

Figure S3. a: Detailed lithological log, **b:** structures, **c:** types of laminations, **d:** grain-size data, **e:** presence of granules 2-3mm, **f**: visually observed microfossils (trace amounts), **g:** main facies distribution, **h:** sharp contacts between facies, **i**: magnetic susceptibility (MS). Note core gaps between different cores due to discontinuous coring (//). M: Mudstone, St: Siltstone: Sd Sandstone.

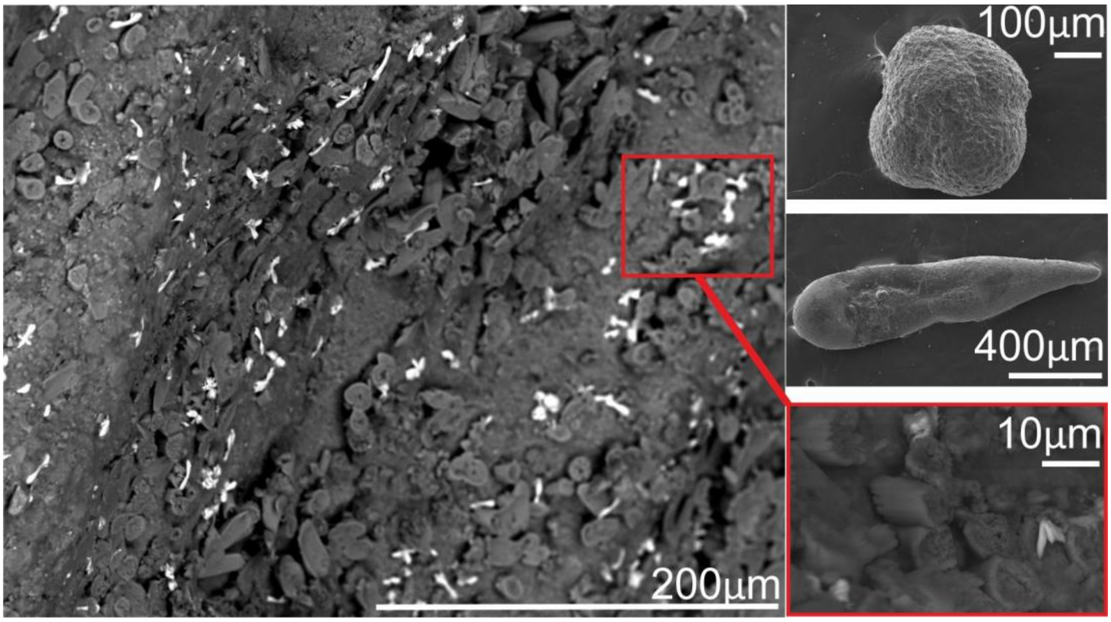

Figure S4. HR-SEM image showing calcareous microfossils associated with barite and representative species of foraminifers found in cores 8R and 9R.

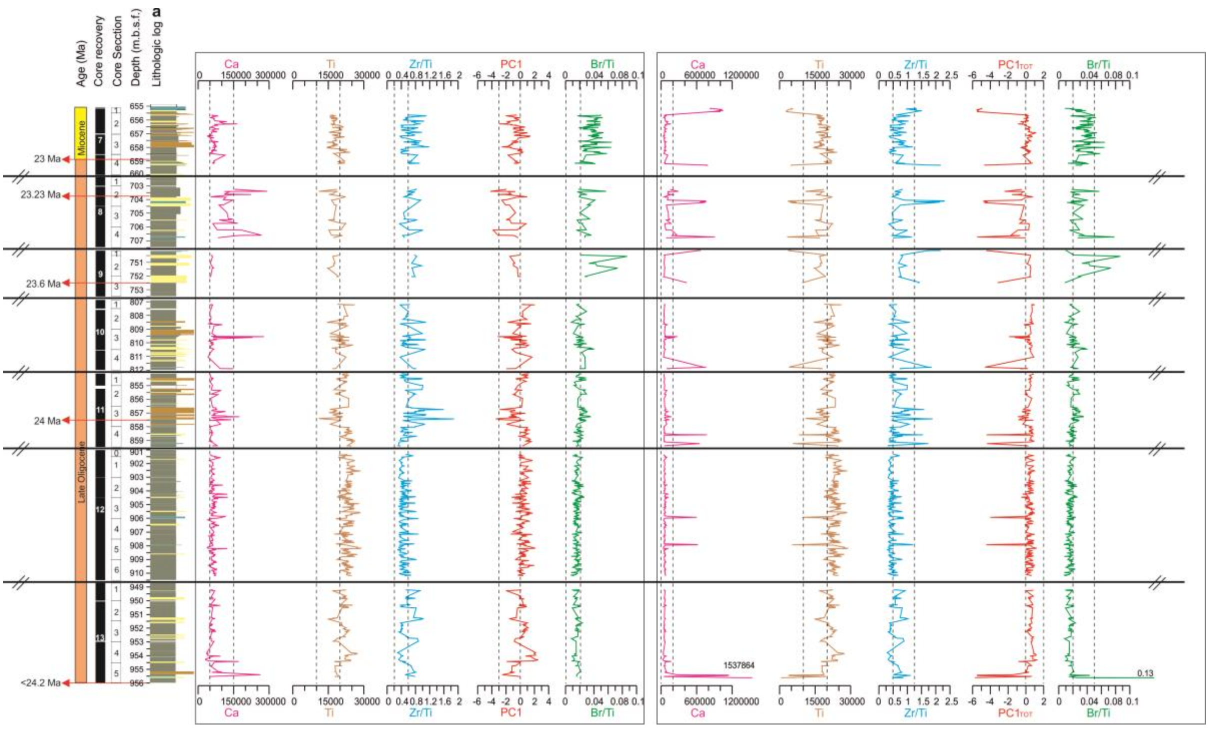

Figure S5. Lithologic log (a) and down-core variations of (i) selected XRF-scanning data (in total counts), elemental ratios and PC1 without the carbonate-cemented facies (left) and (ii) selected XRF-scanning data, elemental ratios and $PC1_{TOT}$ with the carbonate-cemented facies (right). Note core gaps between different cores due to discontinuous coring (//).

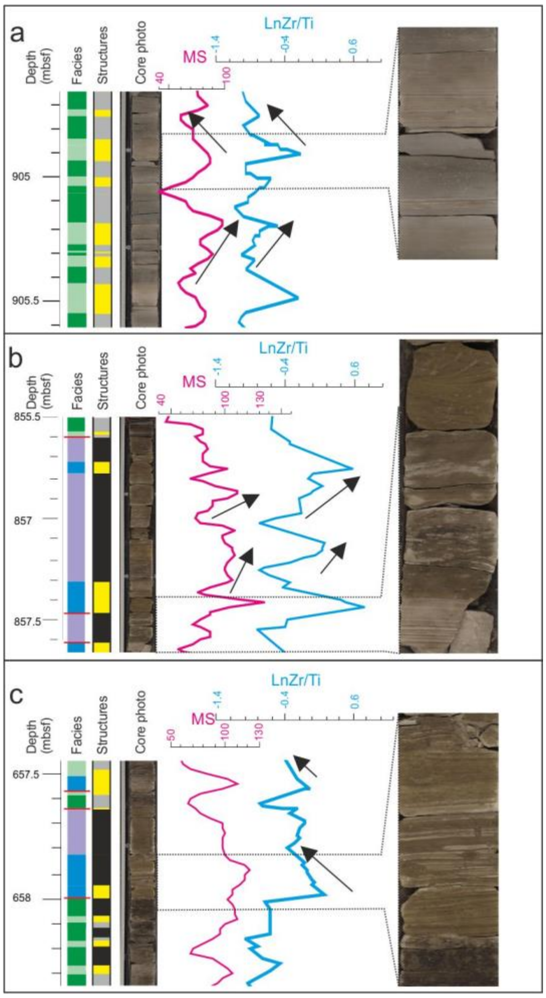

Figure S6. Representative examples of facies associations, including structures, magnetic susceptibility (MS) and Zr/Ti data. **a:** Fine-grained facies associations. **b** and **c:** Coarse-grained facies associations. Arrows indicate inverse and normal grading patterns. Red lines between facies indicate sharp bed contacts. Facies colour and structure codes are given in Figure 3.

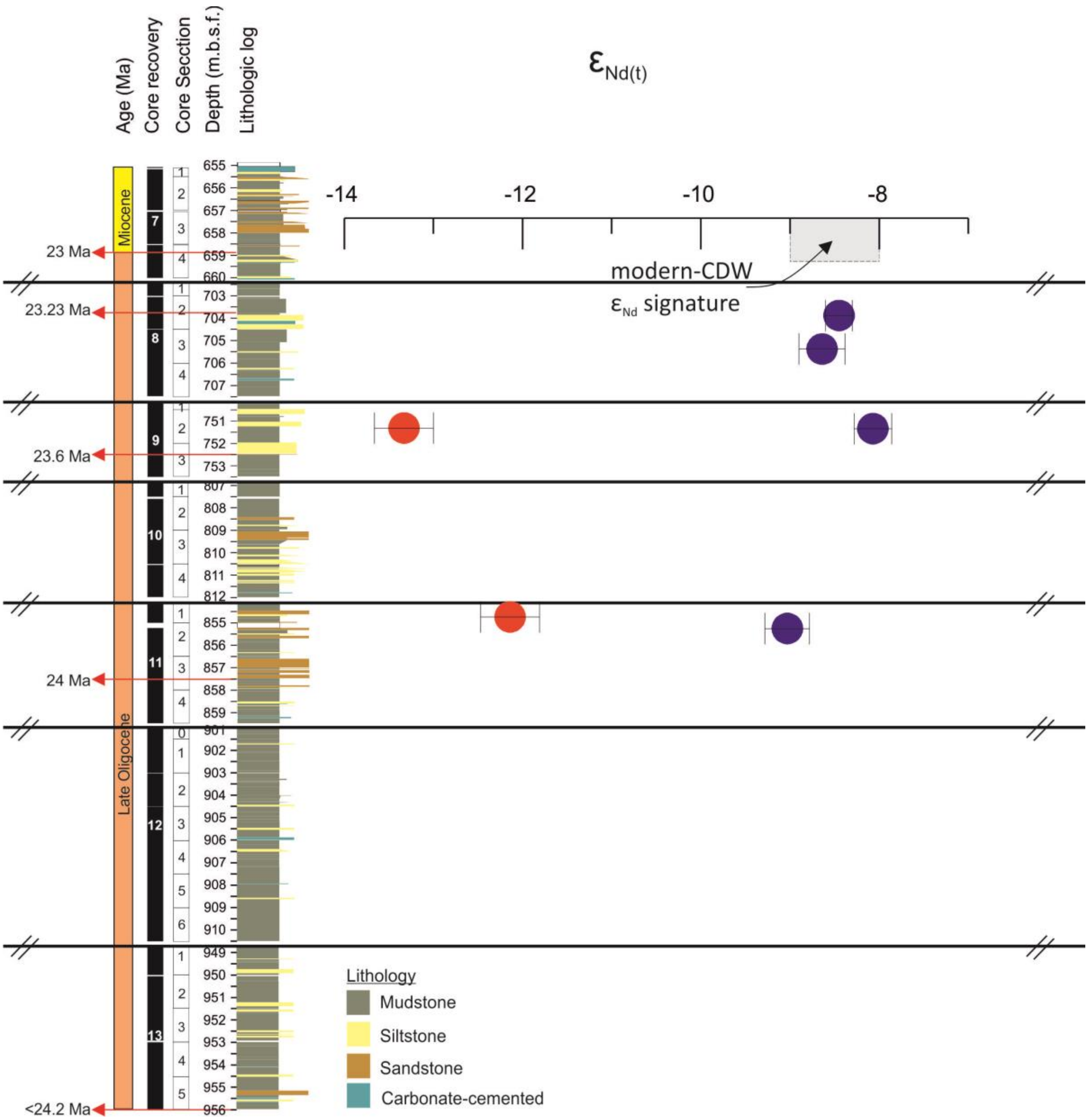

Figure S7. Neodymium isotopic composition of fish debris (blue) and bulk detrital sediment ε_{Nd} values (red) from Hole 269A

Supplementary tables

Table S1. Paleomagnetic dataset at Hole 269A Cores 7R-13R

Leg	Site	Hole	Core	Section	Top (cm)	Bot (cm)	Depth (mbsf)	Sample Name	Declination	Inclination	Intensity (A/m2)	Strat	MAD	Forced	Type	Coordinates	Bedding Strike	Bedding Dip	Num Step	Min Step	Max Step
28	269	A	13	1	53	55	949.03	di1	53.76352373	-5.199547693	12816.60013	7	4.408449078	TRUE	dir	Geographic Coordinates	90	0	5	15	35
28	269	A	13	1	76	78	949.26	di2	187.5173705	-13.90078791	6251.883574	6	3.301610054	TRUE	dir	Geographic Coordinates	90	0	11	25	100
28	269	A	13	1	114	116	949.64	di3	140.0669862	-6.894508896	6266.399988	5	1.729861671	TRUE	dir	Geographic Coordinates	90	0	12	15	90
28	269	A	13	2	44	46	950.44	di4	62.01754422	-27.06342913	16272.10342	4	1.777811659	TRUE	dir	Geographic Coordinates	90	0	12	20	100
28	269	A	13	2	95	98	950.95	di5	139.5556692	42.02077811	14790.02487	3	1.980377917	TRUE	dir	Geographic Coordinates	90	0	14	10	100
28	269	A	13	3	13	15	951.63	di6	99.02692451	28.92119504	9137.591091	2	2.41338962	TRUE	dir	Geographic Coordinates	90	0	8	25	70
28	269	A	13	3	104	106	952.54	di7	182.0068096	24.78570975	11344.96448	1	1.967135126	TRUE	dir	Geographic Coordinates	90	0	12	15	90
28	269	A	13	4	3	5	953.03	di8	222.6946459	19.20222119	5656.079284	8	2.106426055	TRUE	dir	Geographic Coordinates	90	0	9	30	90
28	269	A	13	4	82	84	953.82	di9	35.35353282	26.65869667	4713.510042	7	4.291701509	TRUE	dir	Geographic Coordinates	90	0	8	30	80
28	269	A	13	5	67	69	955.17	di10	43.23591546	-10.24051787	1349.560528	6	13.32826152	TRUE	dir	Geographic Coordinates	90	0	6	5	30
28	269	A	12	cc	108	110		di11	98.56922818	42.67535279	23715.78417	5	2.340095871	TRUE	dir	Geographic Coordinates	90	0	9	20	70
28	269	A	12	1	31	33	901.81	di12	330.0166967	-47.4554181	9962.928043	4	2.367538165	TRUE	dir	Geographic Coordinates	90	0	10	10	60
28	269	A	12	1	100	105	902.5	di13	308.9936867	28.80580856	4401.981022	3	22.37747839	TRUE	dir	Geographic Coordinates	90	0	7	30	70
28	269	A	12	2	55	58	903.55	di14	255.5246598	26.24829681	21456.26987	2	3.458319655	TRUE	dir	Geographic Coordinates	90	0	8	25	70
28	269	A	12	2	99	102	903.99	di15	43.87058825	17.08826976	33370.27581	1	1.930333287	TRUE	dir	Geographic Coordinates	90	0	10	25	90
28	269	A	12	3	31	37	904.81	di16	311.4540766	25.38271471	6261.890212	8	7.110635407	TRUE	dir	Geographic Coordinates	90	0	3	70	100
28	269	A	12	3	100	104	905.5	di17	112.8863995	-20.79215717	21881.08232	7	2.435042272	TRUE	dir	Geographic Coordinates	90	0	9	20	70
28	269	A	12	3	139	143	905.89	di18	28.96001016	-64.21128488	18086.04801	6	2.041162135	TRUE	dir	Geographic Coordinates	90	0	9	20	70
28	269	A	12	4	35	38	906.35	di19	141.8096984	27.06084292	19862.01544	5	3.18722628	TRUE	dir	Geographic Coordinates	90	0	8	25	70
28	269	A	12	4	114	116	907.14	di20	344.1505266	24.98480412	7524.080645	4	5.534615148	TRUE	dir	Geographic Coordinates	90	0	7	15	50
28	269	A	12	5	52	54	908.02	di21	69.08596658	24.27440215	17408.94553	3	2.165969334	TRUE	dir	Geographic Coordinates	90	0	9	25	80
28	269	A	12	6	43	46	909.43	di22	281.6904156	26.9239216	14765.06822	2	2.552548953	TRUE	dir	Geographic Coordinates	90	0	5	40	70
28	269	A	12	6	119	120	910.19	di23	153.9393002	-43.82377169	17273.54343	1	3.971015509	TRUE	dir	Geographic Coordinates	90	0	8	25	70
28	269	A	11	1	128	131	854.78	di24	149.0593065	59.0440706	6141721.081	8	13.68602895	TRUE	dir	Geographic Coordinates	90	0	4	50	80
28	269	A	11	2	100	102	856	di25	326.9019884	-50.97461873	289344012	7	3.08101949	TRUE	dir	Geographic Coordinates	90	0	9	30	90
28	269	A	11	3	116	119	857.66	di26	334.5364202	-50.21976757	388489949.3	6	2.845164352	TRUE	dir	Geographic Coordinates	90	0	11	25	100
28	269	A	11	4	102	104	859.02	di27	226.1544957	-78.90314623	98982659.64	5	1.643774787	TRUE	dir	Geographic Coordinates	90	0	7	30	70
28	269	A	10	1	118	120	807.18	di28	127.4962079	33.84819793	125506107.5	4	3.888959636	TRUE	dir	Geographic Coordinates	90	0	8	25	70
28	269	A	10	2	135	137	808.85	di29	358.1326336	65.43141803	34389970.9	3	4.194877001	TRUE	dir	Geographic Coordinates	90	0	9	30	90
28	269	A	10	3	79	81	809.79	di30	263.7014199	65.84537641	218693976.6	2	1.907142101	TRUE	dir	Geographic Coordinates	90	0	8	30	80
28	269	A	10	3	113	115	810.13	di31	312.9883864	27.39953287	639061206.2	1	0.796159944	TRUE	dir	Geographic Coordinates	90	0	9	30	90
28	269	A	10	4	47	49	810.97	di32	281.4697077	18.89465352	1001907661	8	1.089722914	TRUE	dir	Geographic Coordinates	90	0	9	30	90
28	269	A	9	1	140	141	750.4	di33	6.985047386	37.39524076	71105293.91	7	7.206328365	TRUE	dir	Geographic Coordinates	90	0	6	35	70
28	269	A	9	2	91	92	751.41	di34	142.4203434	12.32332113	310016716.7	6	2.480805913	TRUE	dir	Geographic Coordinates	90	0	9	35	100
28	269	A	9	3	56	57	752.56	di35	30.53633776	51.30379385	222359261.8	5	9.025097405	TRUE	dir	Geographic Coordinates	90	0	7	40	90
28	269	A	9	3	82	84	752.82	di36	148.2317044	28.23487618	320725804.9	4	2.837413	TRUE	dir	Geographic Coordinates	90	0	9	30	90
28	269	A	8	1	112	114	702.62	di37	296.5709821	-35.97232585	178226512.9	3	2.017011139	TRUE	dir	Geographic Coordinates	90	0	6	30	60
28	269	A	8	2	32	34	703.32	di38	178.8055694	-33.57064374	31276157.15	2	15.17208249	TRUE	dir	Geographic Coordinates	90	0	6	35	70
28	269	A	8	3	21	23	704.71	di39	136.2052788	65.45985345	254911417.1	1	1.883407029	TRUE	dir	Geographic Coordinates	90	0	8	30	80
28	269	A	8	4	24	26	706.24	DI40	154.1991718	-55.21781411	125870874.8	8	5.107651031	TRUE	dir	Geographic Coordinates	90	0	8	25	70
28	269	A	7	2	28	30	655.78	DI42	199.0415962	-18.28783989	71590755.93	7	6.586390491	TRUE	dir	Geographic Coordinates	90	0	3	15	25
28	269	A	7	3	21	23	657.21	DI43	193.5689914	-36.21456441	77389858.44	6	1.903325393	TRUE	dir	Geographic Coordinates	90	0	6	35	70
28	269	A	7	4	51	53	659.01	DI44	168.0187196	-26.12330831	72845114.34	5	6.719835872	TRUE	dir	Geographic Coordinates	90	0	4	40	60

1270 **Table S2.** Palynomorphs assemblages at Hole 269A; Cores 7R-13R.

1271

Sample Name	Core Section	Interval (cm)	Depth core (mbsf)	Lycopodium	Lycopodium counted	Weight (g)	Brigantedinium spp.	Brigantedinium cavate	Brigantedinium pynei	Selenopemphix spp.	Selenopemphix antarctica	Selenopemphix Nephroides	Selenopemphix Undulata	Lejeunecysta spp.	Lejeunecysta acuminata	Protoperidinium	Malvinia escutiana	Vozzhennikovia spp.	Spinidinium spp.	Spinidinium macmurdoense	Wetzellia spp.	Rhombodinium draco	Deflandrea spp.	Deflandrea antarctica	Phthanoperidinium spp.	**Total protoperidinioids**
DSDPLeg 28 Site 269A	006R 3W	100-104	610.52	20848	2549	19.4551	9												1							10
DSDP Leg 28 Site 269A	007R 2W	30-34	655.82	20848	648	18.9571	174	1	1	2		3		4	1	9										195
DSDP Leg 28 Site 269A	007R 4W	30-34	658.82	20848	1538	20.0307	127	14						2.5				10	1	2						156.5
DSDP Leg 28 Site 269A	007R 4W	113-117	659.65	20848	2533	19.4604	49	7		1						2		3.5								62.5
DSDP Leg 28 Site 269A	008R 2W	131-135	704.33	20848	2283	20.1364	1											1								2
DSDP Leg 28 Site 269A	008R 3W	28-32	704.8	20848	2243	19.3753	124	15		7				13.5				5	3							167.5
DSDPLeg 28 Site 269A	009R 2W	26-30	750.78	20848	3505	16.3358	45	4											2		1		4	1		59
DSDP Leg 28 Site 269A	009R 3W	30-34	752.32	20848	1863	19.8009																				0
DSDP Leg 28 Site 269A	009R 3W	125-129	753.27	20848	2285	18.2004	86	2		3				10			3	62.5	2	2			1			171.5
DSDP Leg 28 Site 269A	010R 3W	25-29	809.27	20848	2017	20.1234																				0
DSDP Leg 28 Site 269A	010R 4W	25-29	810.77	20848	1999	19.1668	65			3				5.5												73.5
DSDP Leg 28 Site 269A	011R 1W	75-79	854.27	20848	1766	14.4943	187			7	1			2		1										198
DSDP Leg 28 Site 269A	011R 4W	22-26	858.24	20848	2128	20.0815	82	8		7		0.5		6				4.5								108
DSDPLeg 28 Site 269A	011R 4W	125-129	859.27	20848	2100	20.0162	150	25		4								1	1							181
DSDP Leg 28 Site 269A	012R 2W	35-39	902.87	20848	1865	19.4047	88											2								90
DSDP Leg 28 Site 269A	012R 2W	125-129	903.77	20848	2018	20.0258	123	5		6				0.5			1	14	3	1		1	1		1	156.5
DSDPLeg 28 Site 269A	012R 6W	125-129	909.77	20848	2069	20.0322	169	2		20.5		14		4			3	2				1				215.5
DSDPLeg 28 Site 269A	013R 1W	33-37	948.85	20848	840	19.2824	134			19		44		1		1		1								200
DSDP Leg 28 Site 269A	013R 2W	26-30	950.28	20848	1642	20.0555	159.5			35		29.5		1	1											226
DSDP Leg 28 Site 269A	013R 4W	125-129	954.27	20848	839	18.1817	148			26	5	43.5		5					1							228.5

1272

1273

1274

			1					1					2		1					Achomosphaera spp.
		1								1								1		Aiora fenestrata
													1							Areoligera spp.
2	1		7	2		3					1		1		1		1		8	Batiacasphaera spp.
													1		4					Corrudinium spp.
										1									2	Cerebrocysta ssp.
																				Ectosphaeropsis burdigalensis
4	1		2	12	2.5		14	1		6	9	2	9	4	4,5+2			1	1	Enneadocysta spp. "pale"
	3		4	5.5	2.5	1			1	6.5	2		17			3	1		2	Enneadocysta spp. "yellow"
	6	1				1				1	3		9							Gelatia inflata
													1							Homotryblium spp.
	2		2	2	4	1		1			1	2	6	4	5	5	1		16	Impagidinium spp.
													1							Impagidinium spp. Bruin
								1				4	3	2	1		1			Impagidinium aculeatum
1	6			3		6	1							2		3			18	Impagidinium pallidum
			1							1					6				25	Impagidinium cf pallidum
				2																Impagidinium cf paradoxum
			2									4								Impagidinium patulum
3	2																		3	Impagidinium velorum
																				Impagidinium victorianum
								1					1		1			3	16	Nemat. labyrinthus
	3			1		9			2		2					1			13	Pyxidinopsis spp.
3	8	1	2	3	1	1	1				1		1		3				5	Operculodinium spp.
2	3																			Operculodinium centrocarpum
7	8																			Operculodinium "pale"
	1			4																Operculodinium janduchenei
															1				11	Operculodinium piaseckii
10	32																			Operculodinium polar
										1										Operculodinium eirikianum
													1							Operculodinium cf eirikianum
12	4																			Operculodinium "spiky"
10	29						2													Operculodinium wannabe
				2																Reticulatosphaera spp.
1	5			1		1	2				3									Spiniferites spp.
											7									Spiniferites sp A
												1				1				Invertocysta tabulata
																				Invertocysta lacrymosa
54.5	114	2	21	38.5	10	23	20	5	3	17.5	29	13	53.5	12	23	13	4	5	120	**Total gonyaulacoids**
283	340	202	237	195	100	204	128	203	76.5	17.5	201	13	113	180	25	75.5	161	200	130	**Total dinocysts**

Arcritarch present	Pollen present	Bisaccate pollen	Leiosphaera	GDZ	DZS	Brown pollen	Acritarch "spiny"	Acritarch "dotted"	Acritarch "dented"	**Total dinocysts per g**	**P:G**	**P/TOT**
										54.651797	0.0833333	0.0769231
yes ±15	yes	36								339.42786	39	0.975
yes	yes	18	247				7		20	108.61429	39.125	0.9750779
yes ±25	yes	29	350							31.931873	4.8076923	0.8278146
390	yes	5		61						11.337483	0.0869565	0.08
yes	yes	12	443				43		14	86.109515	13.958333	0.9331476
yes ±10	yes	0		243	26					40.962692	1.1028037	0.5244444
										7.3469987	0	0
yes	yes	36	762				5		50	100.51055	5.9137931	0.8553616
										8.9886649	0	0
no	yes	10	311							41.62588	24.5	0.9607843
	yes	23	168	24						165.33793	39.6	0.9753695
	yes	24	583			22				62.446283	5.4	0.84375
<5	yes	17	1106							101.17976	7.8695652	0.8872549
	yes	45	742	43						57.607447	9	0.9
	yes	19	962							100.59768	4.0649351	0.8025641
<5	yes	19	791							118.96149	10.261905	0.9112051
	yes	90	1052							260.00122	100	0.990099
	yes	157	1335							214.93024	1.9911894	0.6656848
	yes	31	175							386.77143	4.1926606	0.8074205

Table S3. Principal components (PC) of Hole 269A; Cores 7R-13R. **a:** PCA $_{TOT}$, **b:** PCA excluding carbonate-cemented intervals.

(a)

PC	Eigenvalue	Variance (%)
PC 1	1.93	63.77
PC 2	0.53	17.50
PC 3	0.26	8.47
PC 4	0.12	3.83
PC 5	0.08	2.48
PC 6	0.06	1.82
PC 7	0.04	1.32
PC 8	0.01	0.35
PC 9	0.01	0.24
PC 10	0.01	0.22
PC 11	0.00	0.00

(b)

PC	Eigenvalue	Variance (%)
PC 1	0.95	34.72
PC 2	0.88	31.98
PC 3	0.27	9.73
PC 4	0.24	8.88
PC 5	0.17	6.19
PC 6	0.09	3.14
PC 7	0.07	2.55
PC 8	0.04	1.41
PC 9	0.02	0.78
PC 10	0.02	0.62
PC 11	0.00	0.00

.

Table S4. Concentrations of GDGTs at Hole 269A; Cores 7R-13R. All samples and corresponding depths, GDGT peak area values, TEX86 (Schouten et al., 2002) and BIT index values (Hopmans et al., 2004), Methane Index (Methzhang) values (Zhang et al., 2011), GDGT2/Crenarchaeol ratios (Weijers et al., 2011), GDGT-0/Crenarchaeol ratios (Blaga et al., 2009) and GDGT-2/GDGT-3 ratios (Taylor et al., 2013), and RING index (Sinninghe Damsté, 2016). Discarded samples (OUTLIER=TRUE) with outlier values are based on BIT > 0.4, GDGT2/GDGT3` > 5, `GDGT0/cren` > 2 and `Methzhang` > 0.3.

Sample code	Depth(mbsf)	GDGT-0	GDGT-1		GDGT-2	GDGT-3	GDGT-4	GDGT-4'	GDGT-IIIa	GDGT-IIIa'	SUM GDGT-IIIa	GDGT-IIa	GDGT-IIa'	SUM GDGT-IIa	GDGT-IIb
		1302	1300	H1300	1298	1296	1292	1292'	1050-1	1050-2	1050-tot	1036-1	1036-2	1036-tot	1034-1
28-269A-7R-2W 30-34cm	655.8	2942750.0	159364.0	0.0	62727.9	18918.3	2706500.0	45714.4	47578.7	26296.1	73874.8	18699.4	13806.1	32505.5	6965.0
28-269A-7R-3W 136-136cm	658.4	12613497.0	717051.9	119649.4	385648.6	77529.1	12553429.0	198797.5	314790.5	156020.8	470811.3	67665.6	73249.0	140914.6	52635.8
28-269A-7R-4W 127-131	659.8	28695870.0	829447.3	248715.4	461230.4	57143.8	8250699.5	231671.9	139414.0	94517.9	233931.9	51122.1	38731.7	89853.8	32993.8
28-269A-8R-3W 142-146	705.9	4760829.0	204032.7	38097.8	92975.4	29892.9	4139520.5	56135.2	167024.0	105912.6	272936.6	90077.1	50242.6	140319.7	54628.9
28-269A-9R-2W 106-110cm	753.1	17138900.0	576784.9	167579.6	251321.1	117106.8	16933678.0	174104.2	230212.3	147753.3	377965.6	70443.5	65665.1	136108.6	69136.6
28-269A-10R-3W 25-28cm	809.3	28890.9	2495.0	7904.5	2223.6	2104.2	4668.5	2071.6	5271.6	2961.4	8233.0	3065.6	5508.6	8574.2	0.0
28-269A-10R-3W 116-120cm	810.2	6003169.0	254334.4	56686.4	86115.8	45950.0	6143775.5	83228.2	151393.5	86406.7	237800.2	52180.1	44458.8	96638.9	42485.1
28-269A-11R-1W 75-79cm	854.3	795513.0	42238.5	0.0	15689.7	5634.5	861324.0	12810.7	19932.8	10570.1	30502.9	8328.0	4752.0	13079.9	5463.0
28-269A-11R-3W 23-27cm	856.8	33051.7	2651.7	0.0	2004.7	2018.5	22133.5	2057.4	9372.8	7193.4	16566.2	3557.1	4061.8	7618.9	0.0
28-269A-12R-2W 40-43cm	902.9	194355.7	10943.2	0.0	3960.4	2268.3	183369.7	4365.3	7947.7	9103.8	17051.5	5069.7	6338.1	11407.8	2383.1
28-269A-12R-4W 25-28cm	905.8	3728442.0	168857.0	33074.1	70626.6	29034.4	3919071.8	48228.7	144021.0	79521.6	223542.6	68037.8	46249.2	114287.0	31120.5
28-269A-12R-4W 125-128cm	906.8	3072708.0	130516.6	16421.6	59769.3	22098.5	3129816.3	44337.4	76395.4	44885.9	121281.3	39721.6	24584.5	64306.1	21236.2
28-269A-13R-1W 33-37cm	948.9	459448.0	21973.4	0.0	7378.4	3209.4	486734.0	6502.2	25618.2	14374.4	39992.6	14912.4	9208.5	24120.9	6242.0
28-269A-13R-2W 87-91cm	950.9	2347130.0	105004.3	0.0	51535.6	19066.5	2323012.3	33990.5	168605.3	101849.8	270455.1	92141.9	50565.0	142706.9	41430.6
28-269A-13R-4W 13-17cm	953.2	2251815.8	122400.4	21870.6	52940.5	18491.2	2273169.8	37531.8	98155.3	57310.7	155466.0	54374.1	31827.6	86201.7	28874.5

GDGT-IIb'	SUM GDGT-IIb		GDGT-IIc	GDGT-IIc'	SUM GDGT-IIc	GDGT-Ia	GDGT-Ib					GDGT-Ic	TEX86	SST	BIT	SUM.ISO	FA1302.ISO	FA1300.ISO	FA1298.ISO
1034-2	1034-tot	OH-1034	1032-1	1032-2	1032-tot	1022	1020	OH-1020a	OH-1020b	OH-1020c	OH-1020d	1018							
14544.7	21509.7	0.0	3749.1	9198.9	12948.0	40162.4	14362.6	0.0	0.0	0.0	0.0	12066.1	0.44	9.60	0.05	5935974.60	0.496	0.027	0.011
80306.2	132942.0	104047.4	13712.3	24680.3	38392.6	259286.0	48214.7	9688.9	309723.9	389706.7	31440.2	44094.6	0.48	12.52	0.06	26545953.10	0.475	0.027	0.015
35129.8	68123.6	37714.4	9001.3	13210.8	22212.1	115207.8	21693.6	12370.7	161634.8	228429.3	19674.6	17263.1	0.47	12.10	0.05	38526062.90	0.745	0.022	0.012
37768.2	92397.1	48924.1	13229.0	14742.5	27971.5	195084.8	29822.2	6062.6	214955.1	307641.0	14341.2	26600.7	0.47	11.49	0.13	9283385.70	0.513	0.022	0.010
69015.9	138152.5	55351.3	22621.5	25153.8	47775.3	379003.8	51333.5	18512.8	350091.6	461749.2	22602.7	47889.6	0.48	12.90	0.05	35191895.00	0.487	0.016	0.007
0.0	0.0	0.0	0.0	0.0	0.0	5851.6	2279.7	2355.4	31366.7	41509.1	9545.0	2403.8	0.72	32.04	0.83	42453.80	0.681	0.059	0.052
34092.4	76577.5	47095.5	10714.1	14235.1	24949.2	167211.4	23949.2	3173.1	198778.5	257938.0	11349.6	19038.2	0.46	10.76	0.08	12616572.90	0.476	0.020	0.007
4166.0	9629.0	0.0	1101.0	1475.0	2576.0	15798.4	2882.8	0.0	0.0	0.0	0.0	1790.2	0.45	9.83	0.06	1733210.38	0.459	0.024	0.009
0.0	0.0	0.0	0.0	0.0	0.0	3545.1	0.0	2460.4	41030.8	52970.5	19288.3	0.0	0.70	30.15	0.56	63917.50	0.517	0.041	0.031
4796.7	7179.8	0.0	2537.9	0.0	2537.9	0.0	3250.4	2962.9	48828.5	58378.8	5677.2	3067.2	0.49	13.49	NA	399262.60	0.487	0.027	0.010
25491.3	56611.8	58382.1	7456.9	9845.0	17301.9	160392.1	17823.1	4769.6	113524.4	137038.3	8631.3	11332.4	0.47	11.45	0.11	7964260.50	0.468	0.021	0.009
17262.9	38499.1	21836.9	7235.3	6543.2	13778.5	102277.7	15114.2	3591.8	77430.9	100388.7	8322.0	10313.6	0.49	13.47	0.08	6459246.10	0.476	0.020	0.009
5069.5	11311.4	0.0	1511.2	1574.5	3085.7	25200.1	3997.7	0.0	0.0	0.0	0.0	1824.3	0.44	9.06	0.16	985245.36	0.466	0.022	0.007
27951.3	69381.9	0.0	10227.7	11422.2	21649.9	151594.1	26127.8	3518.7	56499.7	79548.7	7004.6	11069.5	0.50	14.07	0.20	4879739.20	0.481	0.022	0.011
21519.9	50394.4	0.0	5752.5	7663.4	13415.9	111762.2	16782.5	4996.4	84776.7	101662.3	12490.3	8417.6	0.47	11.78	0.13	4756349.50	0.473	0.026	0.011

FA1296.ISO	FA1292.ISO	FA1292'.ISO	GDGT2/GDGT3	GDGT2/cren	GDGT0/cren	Methzhang	RING	SUM.ALL	SUM.BR	CBT	pH	MBT	MAT	outlierBIT	outlierGDGT2/3	outlierGDGT0/cren	outlierMethzhang	outlierRING	OUTLIER
0.003	0.456	0.008	3.316	0.023	1.087	0.081	1.912	5902393.59	207429.19	0.116	8.350	0.321	10.104	FALSE	FALSE	FALSE	FALSE	FALSE	FALSE
0.003	0.473	0.007	4.974	0.031	1.005	0.085	1.986	26500379.30	1134655.80	0.019	8.603	0.310	10.310	FALSE	FALSE	FALSE	FALSE	FALSE	FALSE
0.001	0.214	0.006	8.071	0.056	3.478	0.137	0.931	37746527.30	568285.90	0.094	8.407	0.271	8.686	FALSE	TRUE	TRUE	FALSE	TRUE	TRUE
0.003	0.446	0.006	3.110	0.022	1.150	0.072	1.859	9741617.30	785132.60	0.144	8.278	0.320	9.926	FALSE	FALSE	FALSE	FALSE	FALSE	FALSE
0.003	0.481	0.005	2.146	0.015	1.012	0.052	1.985	35424911.10	1178228.90	-0.005	8.664	0.406	13.419	FALSE	FALSE	FALSE	FALSE	FALSE	FALSE
0.050	0.110	0.049	1.057	0.476	6.188	0.503	0.947	62973.30	27342.30	0.678	6.890	0.385	8.912	TRUE	FALSE	TRUE	TRUE	TRUE	TRUE
0.004	0.487	0.007	1.874	0.014	0.977	0.058	2.019	12876337.30	646164.60	0.079	8.446	0.325	10.446	FALSE	FALSE	FALSE	FALSE	FALSE	FALSE
0.003	0.497	0.007	2.785	0.018	0.924	0.068	2.070	1745906.93	76259.23	0.106	8.377	0.268	8.532	FALSE	FALSE	FALSE	FALSE	FALSE	FALSE
0.032	0.346	0.032	0.993	0.091	1.493	0.216	1.713	NA	NA	NA	NA	NA	NA	TRUE	FALSE	FALSE	FALSE	TRUE	TRUE
0.006	0.459	0.011	1.746	0.022	1.060	0.084	1.945	NA	NA	0.148	8.268	NA	NA	NA	FALSE	FALSE	FALSE	FALSE	TRUE
0.004	0.492	0.006	2.433	0.018	0.951	0.063	2.042	8297033.40	601290.90	0.249	8.004	0.315	9.170	FALSE	FALSE	FALSE	FALSE	FALSE	FALSE
0.003	0.485	0.007	2.705	0.019	0.982	0.063	2.015	6612432.20	365570.50	0.171	8.208	0.349	10.672	FALSE	FALSE	FALSE	FALSE	FALSE	FALSE
0.003	0.494	0.007	2.299	0.015	0.944	0.062	2.050	1062216.84	109532.69	0.264	7.965	0.283	8.093	FALSE	FALSE	FALSE	FALSE	FALSE	FALSE
0.004	0.476	0.007	2.703	0.022	1.010	0.069	1.986	5397118.00	692985.20	0.247	8.009	0.272	7.853	FALSE	FALSE	FALSE	FALSE	FALSE	FALSE
0.004	0.478	0.008	2.863	0.023	0.991	0.077	2.003	5004957.70	442440.30	0.186	8.169	0.310	9.354	FALSE	FALSE	FALSE	FALSE	FALSE	FALSE

R-script: GDGT Peak area calculation

required packages

```
library(caTools)
library(ggplot2)
library(dplyr)
##
## Attaching package: 'dplyr'
## The following objects are masked from 'package:stats':
##
## filter, lag
## The following objects are masked from 'package:base':
##
## intersect, setdiff, setequal, union
library(readr)
library(readxl)
library(tidyverse)
## ── Attaching packages ─────────────────────────────────────── ─ tidyverse 1.2.1 ──
## ✔ tibble 2.1.3 ✔ purrr 0.3.2
## ✔ tidyr 0.8.3 ✔ stringr 1.3.1
## ✔ tibble 2.1.3 ✔ forcats 0.3.0
## ── Conflicts ────────────────────────────────────────── tidyverse_conflicts() ──
## ✖ dplyr::filter() masks stats::filter()
## ✖ dplyr::lag() masks stats::lag()
library(plotly)
##
## Attaching package: 'plotly'
## The following object is masked from 'package:ggplot2':
##
## last_plot
## The following object is masked from 'package:stats':
##
## filter
## The following object is masked from 'package:graphics':
##
## layout
library(ggtern)
## --
## Remember to cite, run citation(package = 'ggtern') for further info.
## --
##
## Attaching package: 'ggtern'
## The following objects are masked from 'package:ggplot2':
##
## %+%, aes, annotate, calc_element, ggplot, ggplot_build,
## ggplot_gtable, ggplotGrob, ggsave, layer_data, theme,
## theme_bw, theme_classic, theme_dark, theme_gray, theme_light,
## theme_linedraw, theme_minimal, theme_void
theme = theme_set(theme_classic())
library(readxl)
setwd("~/Documents/Projects/Site 269")
```

```
OGdata <- read_excel("269 OG.xlsx")
#shows data tables below
OGdata
adds collumns with calculations from GDGT peak areas
#adds collumns with calculations from GDGT peak areas
OGdata <- OGdata %>%
mutate(
#TEX86 ratio from Schouten et al. 2002
TEX86 = (`1298` + `1296` + `1292'`)/(`1300` + `1298` + `1296` + `1292
'`),
#SST calibrations from Kim et al., 2010; TEX86 linear calibration model (0 m)
SST = 81.5*TEX86 -26.6,
#Hopmans et al. 2004
BIT = (`1050-tot` + `1036-tot` + `1022`)/(`1292` + `1050-tot` + `1036
-tot` + `1022`),
#fractional abundances needed for the RING index
SUM.ISO = `1302` + `1300` + `1298` + `1296` + `1292` + `1292'`,
FA1302.ISO = `1302` / SUM.ISO,
FA1300.ISO = `1300` / SUM.ISO,
FA1298.ISO = `1298` / SUM.ISO,
FA1296.ISO = `1296` / SUM.ISO,
FA1292.ISO = `1292` / SUM.ISO,
`FA1292'.ISO` = `1292'` / SUM.ISO,
#depth contribution (Taylor et al., 2013) AOM (Weijers et al., 2011), lake in
situ production (Blaga et al., 2009), methanogenic (Zhang et al.) indices and
the RING index
`GDGT2/GDGT3` = `1298`/ `1296`,
`GDGT2/cren` = `1298` / `1292`,
`GDGT0/cren` = `1302` / `1292`,
`Methzhang` = (`1300` + `1298` + `1296`) / (`1300` + `1298` + `1296`
+ `1292` + `1292'`),
`RING` = FA1300.ISO + 2*FA1298.ISO + 3*FA1296.ISO + 4*FA1292.ISO + 4*
`FA1292'.ISO`,
#Summarizing
SUM.ALL = `1302` + `1292` + `1292'` + `1022` + `1020` + `1018` + `103
6-tot` + `1034-tot` + `1032-tot` + `1050-tot`,
SUM.BR = `1022` + `1020` + `1018` + `1036-tot` + `1034-tot` + `1032-t
ot` + `1050-tot`,
# weijers et al., 2007
CBT = -log10((`1020` + `1034-tot`) / (`1020` + `1036-tot`)),
pH = (3.3283-CBT)/ 0.3847,
MBT = (`1022` + `1020` + `1018`) / SUM.BR,
#Peterse et al., 2012 (MBT' = MBT, because 1048 and 1046 were not integrated)
`MAT` = 0.81 - 5.67*CBT + 31*MBT,
)
CAPDELRI.L <- function(TEX86) -1.15*TEX86 + 2.98*TEX86^2 + 1.49
CAPDELRI.U <- function(TEX86) -0.39*TEX86 + 3.66*TEX86^2 + 1.69
Outlier ruleas for TEX86
#If:
#RING outside CAPDELRI curves,
#GDGT2/GDGT3 > 5 OR,
#GDGT2/cren > 0.1 OR,
#GDGT0/cren > 2 OR,
#BIT > 0.4 OR,
#Methzhang 1300+1298+1296/1300+1298+1296+1292+1292' > 0.3
```

```
#-->
#rejectTEX86
#this adds columns to your dataframe with a logical value (TRUE or FALSE) for
each outlier rule. The final OUTLIER column is added with a logical value for
whether any of the other oulier rule is true
OGdata <- OGdata %>%
mutate(
`outlierBIT` = BIT > 0.4,
`outlierGDGT2/3` = `GDGT2/GDGT3` > 5,
`outlierGDGT0/cren` = `GDGT0/cren` > 2,
`outlierMethzhang` = `Methzhang` > 0.3,
outlierRING = RING<CAPDELRI.L(TEX86) | RING>CAPDELRI.U(TEX86)
,
OUTLIER = `outlierBIT` | `outlierGDGT2/3` | `outlierGDGT0/cre
n` | `outlierMethzhang` | outlierRING
)
#shows new
```

Supplementary References

Biscaye, P.E., 1965. Mineralogy and sedimentation of recent deep-sea clay in the Atlantic Ocean and adjacent seas and oceans. Geol. Soc. Am. Bull.76 (7), 803–832.

Blaga, C.I., Reichart, G.-J., Heiri, O., Damsté, J.S.S., 2009. Tetraether membrane lipid distributions in water-column particulate matter and sediments: a study of 47 European lakes along a north–south transect. *Journal of Paleolimnology*, *41*(3), 523-540

Hopmans, E.C., Weijers, J.W., Schefuß, E., Herfort, L., Damsté, J.S.S., Schouten, S., 2004. A novel proxy for terrestrial organic matter in sediments based on branched and isoprenoid tetraether lipids. *Earth and Planetary Science Letters, 224*(1-2), 107-116.

Huck, C.E., van de Flierdt, T., Bohaty, S.M., Hammond, S.J., 2017. Antarctic climate, Southern Ocean circulation patterns, and deep water formation during the Eocene, Paleoceanography, 32, 674–691. doi: 10.1002/2017PA003135.Koymans, M.R., Langereis, C.G., Pastor-Galan, D., and van Hinsbergen, D.J.J., 2016. Paleomagnetism.org: An online multi-platform open source environment for paleomagnetic data analysis, Computers and Geosciences, Volume 93, Pages 127–137.

Martin, E.E., Haley B.A., 2000 Fossil fish teeth as proxies for seawater Sr and Nd isotopes. Geochim. Cosmochim. Acta 64, 835–847. doi:10.1016/S0016-7037(99)00376-2.

Schouten, S., Hopmans, E.C., Schefuß, E., Damste, J.S.S., 2002. Distributional variations in marine crenarchaeotal membrane lipids: a new tool for reconstructing ancient sea water temperatures? *Earth and Planetary Science Letters, 204*(1-2), 265-274.

Sinninghe Damsté, J.S., 2016. Spatial heterogeneity of sources of branched tetraethers in shelf systems: The geochemistry of tetraethers in the Berau River delta (Kalimantan, Indonesia). Geochimica et Cosmochimica Acta, 186, 13-31, https://doi.org/10.1016/j.gca.2016.04.033

Taylor, K.W., Huber, M., Hollis, C.J., Hernandez-Sanchez, M.T., Pancost, R.D., 2013. Re-evaluating modern and Palaeogene GDGT distributions: Implications for SST reconstructions. *Global and Planetary Change, 108*, 158-174.

Weijers, J.W.H., Lim, K.L.H., Aquilina, A., Sinninghe Damsté, J.S., Pancost, R.D., 2011. Biogeochemical controls on glycerol dialkyl glycerol tetraether lipid distributions in sediments characterized by diffusive methane flux, Geochemistry, Geophysics, Geosystems, 12, 10, https://doi.org/10.1029/2011GC003724

Zhang, Y. G., Zhang, C. L., Liu, X.-L., Li, L., Hinrichs, K.-U., Noakes, J. E., 2011. Methane Index: A tetraether archaeal lipid biomarker indicator for detecting the instability of marine gas hydrates. *Earth and Planetary Science Letters, 307*(3-4), 525-534.